THE ROLE OF THERMAL ENERGY IN SHOCK CONSOLIDATION

M. A. Meyers*, S. S. Shang*, and K. Hokamoto**

*Department of Applied Mechanics and Engineering Sciences
University of California, San Diego
La Jolla, CA 92093-0411, U.S.A.

**Department of Mechanical Engineering
Kumamoto University
Kumamoto 860, Japan

to be published in:

APPLICATIONS OF SHOCK WAVES TO MATERIALS SCIENCE

Edited by Akira B. Sawaoka
Springer Verlag, 1993

CONTENTS

ABSTRACT

Shock consolidation has been applied to a large number of metallic, ceramic, and intermetallic powders over the years. The shock wave deposits energy preferentially at the particle surfaces due to the conversion of kinetic energy into thermal energy, interparticle friction energy, and plastic deformation energy. This temperature rise at the particle surfaces may result in interparticle melting, if conditions are right. Whereas the pressures required to consolidate soft materials are low, these pressures can be exceedingly high for hard materials (intermetallics and ceramics). Tensile pulses generated by reflection/refraction of the primary shock wave therefore interact with existing flaws, activating them and producing fracture. Residual stresses are also a major problem.

Cracking is the major problem encountered in shock consolidated solids. In an effort to eliminate cracking while retaining the unique features of shock consolidation, three novel approaches have been implemented by the authors and co-workers:

1 - Shock consolidation of pre-heated specimens.

2 - Shock densification at a low pressure (just above threshold for pore collapse) followed by hot isostatic pressing or sintering.

3 - Use of local shock-induced reactions to increase temperatures of particle interfaces and enhance bonding.

These techniques were applied to rapidly solidified nickel-base superalloys, titanium and titanium aluminide powder, and to non-oxide ceramics (silicon carbide, cubic boron nitride and diamond). Reduction of cracking was observed with interparticle melting and reactions. Microstructural results and mechanical properties are discussed.

1. Introduction

Dynamic consolidation has considerable potential for densifying high strength materials which are very difficult to sinter by conventional techniques. Formation of dense compacts requires the collapse of the gaps between the particles as well as considerable amount of energy deposited at the particle surfaces for interparticle bonding. The ultra rapid deformation and energy deposition in shock consolidation produces partial melting at the particle surfaces followed by a rapid solidification via heat conduction into the interior of the particles. A series of attempts have been made by a number of investigators to consolidate these difficult-to-consolidate powders [1-6]. However, there exist two major problems. One is cracking of the compacts at both the microscopic and macroscopic level. The other is a lack of uniformity in microstructure and mechanical properties within the resulting compacts. Three novel approaches have been implemented: (1) shock consolidation of pre-heated specimens; (2) shock densification at a low pressure (just above threshold for pore collapse) followed by hot isostatic pressing (hipping); (3) use of local shock-induced reactions to increase temperatures of particle interfaces and enhance bonding. Figure 1 shows, in a schematic fashion, these three approaches.

In this chapter we will present an analysis of the energy deposition processes at the shock front (Section 2). The experimental techniques developed by the authors and co-workers to carry out the explosive consolidation and additional thermal energy application are described in Section 3. In Section 4 the experimental results obtained in shock consolidation experiments of nickel-base superalloys [9], titanium aluminides [7, 11-12], silicides [13], and, silicon carbide, diamond and boron nitride [8] are discussed.

2. Energy Deposition During Shock Processing

It is very important to estimate the total energy needed to consolidate a material and to determine the shock parameters required to effect such a consolidation by shock waves. This predictive capability has been obtained, for soft materials, through the energy flux models of Gourdin [14] and Schwarz *et al.* [15]. For harder materials, the energy expended in plastic deformation becomes an important component of the overall equation and energy predictions incorporating plastic work have been made by Nesterenko [16] and Ferreira and Meyers [20].

In this section the total energy requirement will be calculated for some typical "hard" materials: SiC, c-BN, diamond, and Ti_3Al. This estimate of the overall energy enables us to establish the minimum shock energy required as well as the energy partitioning, when other sources of energy other than shock energy are used.

The discussion presented below is an extension of the work by Schwarz *et al.* [15] and Ferreira and Meyers [20]. Schwarz *et al.* [15] only considered the energy required to produce a melting layer of a specified thickness around the particles. This melting energy was equated to the

shock energy, and a required shock pressure could be in such a manner established. The expression developed by Schwarz *et al.* [15] is:

$$E_m = [\overline{C}_p (T_m - T_0) + H_m] L \qquad (1)$$

where $\overline{C}_p$ is the average specific heat, H_m is the latent heat of fusion, L is the fraction melted, T_m is the melting temperature of the solid material and T_0 its initial temperature.

However, there are other energy dissipation mechanisms at the shock front other than melting at the particle surfaces, and Figure 2 shows schematically the various phenomena occurring during shock compaction. These are:

(a) The material is plastically deformed; the collapse of the voids requires plastic flow. A plastic deformation energy has to be computed.

(b) The plastic flow of the material is a dynamic process, leading to interparticle impact, friction, and plastic flow beyond the flow geometrically necessary to collapse the voids. We will call this component "microkinetic energy"; Nesterenko [16] was the first investigator to consider it.

(c) Melting at interparticle regions: It is known that energy is preferentially deposited at the particle surface, leading eventually to their melting. This is the main component of Schwarz e*t al.* [15].

(d) Defect energy: Point, line, and interfacial defects are produced by the passage of the shock wave; Meyers and Murr [17] provide quantitative assessments of these defect concentrations.

(e) Friction energy: The rearrangement of the powders at the shock front requires relative motions, under the applied stress. Thus, friction may play a role in energy deposition at the shock front.

(f) Fracture energy: Brittle materials may consolidate by fracturing. The comminuted particles can more efficiently fill the voids.

(g) Gas compression: Compaction is most often conducted with the powder being initially at atmospheric pressure. Thus, the gaps between the powders are filled with gas. Shock compaction of the powders compresses and heats these gases. This effect was considered first by Lotrich, Akashi, and Sawaoka [18]. Elliott and Staudhammer [19] demonstrated, by conducting compaction experiments at different gas pressures, the importance of the interparticle gas on shock consolidation.

Some of the energetic contributions given above were used by Ferreira and Meyers [20] to calculate an overall energy expenditure term in shock consolidation. They proposed the simple equation:

$$E_T = E_{v.c.} + E_m + E_d \tag{2}$$

where $E_{v.c.}$, E_m, and E_d are the void collapse, melting, and defect energies. They used the following expressions for the three energy components above:

$$E_{V.C.} = \frac{2}{3} Y V_s \{[\alpha_0 \ln \alpha_0 - (\alpha_0 - 1) \ln (\alpha_0 - 1)] - [\alpha \ln \alpha - (\alpha - 1) \ln (\alpha - 1)]\} \tag{3}$$

where α_0 and α are the initial and final distention of the material, Y is the yield stress and V_s is the solid volume. The distention is defined as the ratio between the specific volumes of the porous and the densified materials. This expression is due to Carroll and Holt [21]. For the melting energy, Ferreira and Meyers [20] subtracted the energy involved in the plastic deformation of the material, i.e., part of the energy is expended in plastic deformation and it should not be computed twice. Therefore, Schwarz *et. al.*'s [15] equation (Eqn. 1) was changed to:

$$E_m = \left[\overline{C}_p \left(T_m - T_0 - \frac{E_{v.c.}}{\overline{C}_p} \right) + H_m \right] L \tag{4}$$

The third component of energy considered by Ferreira and Meyers [20] was the dislocation energy:

$$E_d = \left(\frac{Gb^2}{10} + \frac{Gb^2}{4} \ln \frac{\rho_d^{-1/2}}{5} \right) \frac{\rho_p}{\rho_0} \tag{4A}$$

where G is the shear modulus, b is the Burgers vector, ρ_d is the dislocation density, ρ_p is the powder density, and ρ_0 is the density of the consolidated material. According to the literature [17] one finds that the dislocation density for shock loaded materials in the pressure range where shock consolidation occurs is approximately equal to 5×10^{10} cm^{-2}. The computed value of E_d was found to be negligible.

This energy E_T was equated to the shock energy, E_S, which is equal to:

$$E_S = \frac{P}{2} (V_{00} - V) \tag{5}$$

V_{00} and V are the initial and shock compressed specific volumes, respectively. The relationship between P and V is obtained, for powders, through the equation of state for the solid material and the Mie-Gruneisen equation formulation.

By setting:

$$E_S = E_T$$

it is possible to obtain the pressure required to shock consolidate a powder. The details of these calculations are described elsewhere [20]. The required pressure for shock compaction of different powder materials was calculated at several distentions and the same particle diameter (40 μm), with the hardness values ranging from 1.2 GPa to 98 GPa; from these results one can obtain a master plot. The pressure vs hardness curves were fitted to a line, as shown in Figure 3. The results show that as distention decreases, higher pressure is required to shock consolidate the material. It is also shown that at same melting fraction (same particle diameter) and at same distention, the greater the strength, the greater is the pressure required for shock compaction. Thus as a first approximation, these calculations can be used as a starting point for prediction of the shock consolidation pressures.

More recently, Shang and Meyers [23] have modified the model proposed by Ferreira and Meyers making it more physically realistic. If one looks at Figure 2, one can see that the various mechanisms are not independent. Indeed, the production of a molten layer is the direct consequence of the various processes: void collapse, microkinetic energy, gas heating, interparticle friction. Shang and Meyers [23] proposed an alternative method to estimate the void collapse energy and calculated the microkinetic energy separately. In the computation of the void collapse energy they used the model developed by Helle *et al.* [24].

The void collapse energy is strongly affected by particle geometry, particle contact areas and mechanical properties of the particle and adjacent particle. Two major steps in the development of this model are:

(1) Calculation of the forces transmitted to the contact areas.

(2) Calculation of the total contact area as a function of the relative density.

Fischmeister and Arzt [25] infer that the force transmitted to contact areas is

$$f = 4\pi R^2 P/\rho Z \tag{6}$$

where R is the particle diameter, P the applied stress, ρ the current density and Z the coordination number of the powders. When pressure is applied to a powder compact, this causes the total contact area to increase. The total average area of contact per particle is

$$ZA_c = 4\pi \rho \left(\frac{\rho - \rho_0}{1 - \rho_0}\right) R^2 \tag{7}$$

The effective pressure on each particle contact is

$$P_{eff} = f/A_c = 4\pi R^2 P/A_c Z\rho \tag{8}$$

Using equation (7), the contact pressure is given

$$P_{eff} = \frac{P(1 - \rho_0)}{\rho^2(\rho - \rho_0)} \tag{9}$$

The effect of trapped gas is ignored. The plastic yield condition [26] is assumed to be

$$P_{eff} \geq 2.97\ Y_y \tag{10}$$

Y is the flow stress of the material. The external pressure which will cause plastic yielding is

$$P_y = 2.97\ \rho^2 \frac{(\rho - \rho_0)}{(1 - \rho_0)} Y_y \tag{11}$$

The total energy required to densify the material is given by

$$E_d = \int_{V_0}^{V_f} P_y\, dV = \frac{2.97\ Y_y}{1 - \rho_0} \int_{V_0}^{V_f} V^{-2}\left(V^{-1} - \rho_0\right) dV$$

$$E_d = \frac{2.97\ Y_y}{1 - \rho_0}\left[\frac{(-\rho_f^2 - \rho_0^2)}{2} + \rho_f \rho_0\right] \tag{12}$$

Figure 4(a), (b), (c), and (d) show the external pressure vs specific volume for diamond, c-BN, SiC ad Ti_3Al during the plastic yielding stage (application of Eqn. 11). The overall void collapse energy done on compacting the powder is given by the area under the pressure-volume curve.

Nesterenko [16] developed a model which describes the relative movement of particles under dynamic compression, as shown in Figure 5. In this model, the external shell impacts the central core (with radius c) at an impact velocity of V. This impact velocity is estimated to be

$$V = \frac{\text{average relative movement of particles}}{\text{shock rise time}} \tag{13}$$

For large particle size (50-150 μm), the interstitial void volume is larger than that of small particle size (10-50 μm). Relative movement of particles, upon densification, is greater for large particle size, which causes larger deformation per interstitial site. Furthermore, he defined the dimensions of central core and shell.

$$\alpha_0 = \rho_s / \rho_p$$

$$a_0 = R$$

$$b_0 = R\,\alpha_0^{1/3}$$

$$c = R\,(2 - \alpha_0)^{1/3}$$

where α_0 is the initial distention and R is the average size. The shock rise time can be estimated from Gourdin's model [14]. The impact velocity is given by

$$V = \frac{a_0 - c}{t} \tag{14}$$

therefore, the microkinetic energy is given as

$$E_k = \frac{1}{2} f V^2 = \frac{1}{2} f \left(\frac{a_0 - c}{t}\right)^2 \tag{15}$$

$$f = \frac{b_0^3 - a_0^3}{b_0^3 - a_0^3 + c^3}$$

Staudhammer and Murr [27] have shown that interstitial void volume is strongly dependent on particle size, especially for micron or submicron powders. Figure 6 shows particle size versus actual void volume for monosize spherical powders. For fine particles (<10 μm), larger interstitial void volumes for fine particles will result in larger energy deposition, but relative movement of constrained particle will decrease. Therefore, the effective pressure transmitted to contact areas will decrease; this will reduce shock energy deposited at the powder surfaces. At low shock pressure or for powders with higher initial densities (<50%TD), the shock rise time is longer. From Eqn. 15, it can be seen that the microkinetic energy decreases with increasing of the shock

rise time. Nesterenko's model correctly describes the lack of melting in these compacts due to insufficiency of relative movement of the particles.

Shang and Meyers [33] considered the deformation, microkinetic, and defect energies and computed shock energies. The pressure can be estimated by equating the shock energy (Eqn. 5) with the sum of the energies dissipated (Eqn. 4A, 12, and 15):

$$P = \frac{2\rho_0 \rho}{(\rho - \rho_0)}\left[\left(\frac{Gb^2}{10} + \frac{Gb^2}{4}\ln\frac{\rho_d^{-1/2}}{5}\right)\frac{\rho_P}{\rho_0} + \frac{1}{2}f\left(\frac{a_0 - c}{t}\right)^2 + \frac{2.97\ Y_y}{1 - \rho_0}\left(\frac{-\rho_f^2 - \rho_0^2}{2} + \rho_f \rho_0\right)\right] \qquad (16)$$

Figure 7 shows the predicted pressures required to consolidate materials with different hardnesses incorporating the ideas discussed in the previous paragraphs (Shang and Meyers [23]). The calculations were conducted for four materials: Ti_3Al, SiC, BN, and diamond. Three different distentions (1.18, 1.33, and 1.54) were used. It can be seen that the pressure required is decreased as the distention is increased. These predictions are fairly close, but somewhat lower than the ones obtained by Ferreira and Meyers [20].

In the case of pre-heating or shock-induced reactions, these energetic terms can be incorporated into the overall computation. Thus, the shock energy can be decreased by non-shock energy terms.

3. Experimental Techniques

A wide range of experimental setups have been used over the past thirty years to shock consolidate powders. These systems are grouped into two classes:

1 - explosively driven systems

2 - gas/propellant driven systems

The authors will restrict themselves to the description of the systems that they have used. For detailed descriptions of other systems, the works of Graham [28], Thadhani [29], Korth [30], Vreeland [31], Ahrens [32], Sawaoka [33], Prümmer [34], Staudhammer and Murr [27] should be consulted.

Explosively generated cylindrical and planar systems were used and/or developed at the Center for Explosives Technology Research, New Mexico Tech, Socorro, New Mexico, by Meyers and co-workers [7-13, 35, 36, 38].

3.1 Cylindrical System

The cylindrical system is the most common geometry for shock consolidation because of the ease with which set-ups can be developed. This system has been used by Meyers and co-workers since 1981 [35]. In Europe, it has been used since the 60's. A detailed description is given by Prümmer [34]. A modification of the cylindrical system has been developed by Meyers

and Wang [36] in 1988. Figure 8(a) shows the basic components of this system. The powder is contained in the internal tube. The external tube is surrounded by the explosive charge, which is detonated at one end; this external tube acts as a flyer tube, impacting the internal tube. This technique generates pressures in the powder that can be several time higher than the ones generated by the single tube technique. Thus, low-detonation-velocity explosives can be used to consolidate hard powders, and the formation of the Mach stem is decreased. Significant improvements in compact quality were obtained in nickel-base superalloys [9], titanium alloys [7, 11, 12], and aluminum-lithium alloys [13].

The radial cross-sectional view of the system employing the double tube configuration is shown in Fig. 8(b). By applying an analysis similar to that developed by Gurney [37] for the velocity of fragments, one can estimate the velocity at which the flyer tube is accelerated inwards by the explosive. The chemical energy of the explosive is equated to the sum of the kinetic energy of the gases and that of the tube. One obtains the following equation:

$$V_p = \sqrt{2E}\left(3\Big/\left[5\,(m/c) + 2\,(m/c)\frac{2R + r_0}{r_0} + \frac{2r_0}{R + r_0}\right]\right)^{1/2} \qquad (17)$$

where V_p is the velocity of the flyer tube and m/c is the ratio between the mass of the flyer tube and the mass of the explosive charge. R and r_0 are shown in Fig. 8(b). The importance of this equation is that it allows the selection of a pre-established pressure in the powder. The shock pressure is directly related to the impact velocity.

A schematic of the higher temperature test device is illustrated in Fig. 9(b). The heated powder container is dropped into a mild steel pipe (which acts as the flyer tube) by the release of a solenoid switch). The bottom portion of the mild steel flyer tube (equivalent to the height of the powder container) is surrounded by the explosive charge in a PVC pipe. The charge is initiated at the bottom using a detonator. Prior to the test, the powder container (loaded and sealed under argon atmosphere) is heated in a furnace at the desired temperature and loaded in the test device. Proper precautions are taken to minimize the temperature loss in the powder container by firing the charge in less than three minutes after the hot sample is removed from the furnace. The capsule is propelled upwards by the detonation at the bottom and has to be trapped. An armor plate standing on four support legs (Fig. 9(a)) and having the bottom surface protected by sand bags has been successfully used. This system was developed by Wang *et al.* [9].

A more elaborate system, with enhanced safety features and in which detonation is initiated at the top, is shown in Fig. 9(b). In this system, the hot capsule containing the powder is placed below the explosive charge. A push-tube activated by a counterweight raises the capsule until it penetrates the explosive charge (Fig 9(b)). The system is activated by a solenoid that releases the

push-tube. In case of emergency or failure to detonate, a second safety solenoid drops the counter weight and the capsule is freed to drop from the explosive. This eliminates the possibility of accidental exposure of the explosive to high temperatures for prolonged times. This system was developed by Ferreira *et al.* [11].

3.2 Sawaoka System

Sawaoka and co-workers [1, 2, 33], in Japan, developed a planar impact system using a flyer plate in a planar parallel impact against a target in which capsules with the powders are placed. Very high impact velocity experiments can be conducted for consolidation of certain very hard and difficult-to-bond materials like ceramics. The Sawaoka fixtures utilize explosively driven plates for impact, to generate very high shock pressures (in the range of about 20-100 GPa) [1, 2].

The set-up employs stainless steel flyer plates impacting stainless steel capsules at velocities of 1.5-3.0 km/s. The fixture configuration and the explosive assembly is shown in Fig. 10. The flyer plate is accelerated downwards by the detonation of an explosive charge resting on it top. The explosive charge is initiated simultaneously over the top surface by an explosive system called "mousetrap assembly" or by a plane-wave lens. These set-ups create a plane wave that initiates the detonation at the top surface simultaneously. Up to 8 or 12 individual capsules containing the powder can be utilized, and are held in cavities in the recovery fixture. The shock pressures and temperatures within these capsules are quite inhomogeneous because the powder has a different shock impedance and velocity than the capsule. Computer simulations are used to obtain calculated pressures and temperatures within the capsules [28, 38].

A modification of this system for high-temperature consolidation was developed by Yu and Meyers [38]. The set-up is shown in Figure 10(b). The capsules and surrounding tooling are placed in a discardable furnace, which is heated to the desired temperature. The main explosive charge and plane-wave generator, resting on the flyer plate, are placed on a cart that can descend a 4° ramp, once the solenoid is activated. When the main charge arrives to its final destination it can be detonated. If any problem arises, the charge can be rapidly withdrawn by the activation of solenoid 2, which is a significant safety feature. Pre-shock temperatures as high as 970 K have been achieved by this method. For these high temperatures, the capsule material has to be a nickel-base superalloy instead of stainless steel.

4. Consolidation Experiments: Results and Discussion

Section 2 describes, in a quantitative manner, the energy expenditure in shock consolidation. The problems encountered with shock consolidation are primarily cracking and incomplete bonding. Figure 11(a) shows plots of critical flaw size as a function of tensile stress level for materials having different fracture toughnesses. These plots were made using the well known fracture mechanics equation: $\sigma = K_{IC}\sqrt{\pi a}$. It is difficult to conceive a shock consolidation

process in which no flaws are left, and the particle size is a good indicator of the inherent flaw size in a shock consolidated material. The three fracture toughnesses given, 5, 50, and 100 MPa $\sqrt{m}$, are characteristic of brittle (ceramics), tough (steel, titanium alloys) and very ductile materials (copper, nickel), respectively. Figure 11(b) shows the critical tensile stresses for 25 μm and 10 μm particle sizes as a function of the compressive stresses needed to consolidate the respective powders. The compressive stresses were taken from the calculations given in Section 2 (Eqn. 16), at a distention corresponding to an initial density of 65% of the theoretical density (this is a typical value for powders). Tensile stresses due to reflections are always present in shock consolidation systems. Additional sources of stresses are residual stresses due to the loading inhomogeneity and the temperature gradients during cooling. The amplitude of the reflected tensile stresses can be as high as the compressive stresses. However, in well designed systems a significant portion of the tensile stresses is trapped. When the tensile stresses exceed the critical tensile stresses for the specific material, failure occurs; this is shown in Figure 11(b) in a schematic fashion. A realistic line shows $\sigma_t = 0.1\sigma_c$, i.e., the tensile reflections have, at most, an amplitude of 10% of the compressive pulse. Thus, the hatched region is termed "Danger Zone". By reducing the shock amplitude it is possible to translate the curve downwards, and point [A] (corresponding to a hypothetical material) is changed to [B]. Thus, there are two approaches to be implemented for improved shock consolidation.

(a) reduction of tensile stresses

(b) reduction of shock energy.

This chapter deals exclusively with methods used to decrease the shock energy necessary for consolidation. Shock energy is replaced by thermal or chemical energy in an effort to improve compact quality. In this section, results obtained by the authors using the three approaches delineated in Figure 1 will be discussed.

4.1 Hot Shock Consolidation

Wang, Meyers, and Szecket [9] developed a high temperature shock consolidation system, shown in Figure 9(a), for nickel-base superalloys. Earlier experiments by Meyers, Gupta, and Murr [35], Meyers and Pak [39], and Wang, Meyers, and Graham [40] had yielded good bonding but a great deal of cracking, using a single tube cylindrical geometry. High-temperature shock consolidation experiments were conducted and compared with room-temperature experimental results. As is expected from energetic considerations, the melting fraction increases with temperature, at a constant pressure. The volume fraction of interparticle molten (and resolidified) regions could be established for shock consolidation experiments conducted at different temperatures and pressures, because they etched differently. The results are shown in Figure 12. At a fixed pressure, the molten fraction increases with initial temperature. This is due to both the decrease in flow stress of the material with temperature and to the non-shock energy component

provided by pre-heating the powders. It was possible, by using preheating, to obtain good consolidation of the superalloy with absence of cracking. The best mechanical properties were obtained by pre-heating the specimen to 525°C and using a shock pressure of 18 GPa, resulting in approximately 25% apparent interparticle melting. Tensile tests were conducted and typical results are displayed in Figure 13. Aging of the alloys subsequent to shock consolidation further increased the yield and ultimate tensile strengths.

Ferreira *et al.* [11, 12] shock consolidated titanium aluminides at ambient and high temperatures, using the experimental set-up shown in Figure 9(b). Pre-shock temperatures were 600°C, 750°C, and 900°C. Two basic compositions produced by rapid solidification rate were used: Ti-21 wt pct Nb-14 wt pct Al and Ti-30.9 wt pct Al-14.2 wt pct Nb. These powders exhibit the basic structures of Ti_3Al and TiAl, respectively. The increase in pre-shock temperatures led to a decrease in cracking, in some cases. Figure 14 shows the macrocrack surface area per unit volume for the various conditions. Ti_3Al undergoes a BCC-tetragonal transformation upon heating and this embrittles the original ductile microstructure retained by rapid solidification. This example illustrates the fact that by increasing the pre-shock temperature one can also increase the propensity for cracking.

Diamond, cubic boron nitride and silicon carbide powders were explosively consolidated at high temperature by using a planar impact system (Figure 10). Hot shock consolidated materials exhibited a decrease of surface cracks as compared with specimens consolidated at room temperature. The consolidated diamond specimen showed evidence of surface melting of the particles by small crystallized grains generated during cooling of this molten layer. 4-8 μm diamond consolidated showed good bonding. Excess cracks and generation of graphite were observed by the increase of particle size. Hot consolidated diamond admixed with graphite showed the highest hardness value, but the improvement of the bonding was not confirmed by the specimen admixed with silicon powders. Hot consolidated 40-50 μm c-BN showed good bonding compared with the specimen which has small particles. The improvement of the bonding of c-BN powders by the addition of graphite could not be recognized in this investigation [8]. These results are also described by Shang, Hokamoto, and Meyers [8]. A detailed description is presented in the three following sub-sections A, B, and C.

A. Characterization of Silicon Carbide

Two different sizes of pure SiC powders (7 and 44 μm) were used as starting materials in the high temperature shock experiments. Well consolidated samples were obtained upon shocking preheated SiC powders with 65% of the theoretical density at an impact velocity of 1.9 km/s. The shock pressure was calculated to be 12 GPa by using the one-dimensional impedance matching technique. However, cracking is not totally eliminated and circumferential cracks are noticeable. Scanning electron microscopic (SEM) analysis of recovered SiC compacts revealed that SiC

particles underwent a considerable amount of deformation and the material was fully densified. Figure 15 shows the microstructure of a fracture surface of 7 μm SiC compact. The fractograph indicates that cracks are transgranular and this is evidence for excellent bonding of the powders. The relative densities of the 7 and 44 μm SiC compacts were 98.8% and 98.5% of theoretical, respectively. Both samples had a very close average microhardness value of 28 GPa. Transmission electron microscopic (TEM) analysis (Figure 16) revealed the substructural features of the 44 μm SiC compacts. We can observe lattice distortion in the interior of SiC particle, indicating that the particle was heavily deformed (Figure 16(a)). Figure 16(b) shows the interparticle region. The dark round regions (8-80 nm) in the micrograph are nanocrystalline SiC particles, while the white surrounding material corresponds to the amorphous phase. This interfacial layer was formed due to the very rapid collapse of the gaps between the particles as well as the rapid deposition of energy upon interparticle sliding. Furthermore, this thin interfacial layer (0.2-0.3 μm) and high thermal conductivity of SiC (13 W/m°C) also promote the tendency for these nanocrystalline structure and amorphous phase. The energy deposition time is on the order of the wave transit time through the particle (a few nanoseconds). The melted or sublimated interparticle material resolidifies at cooling rates as high as 10^5 to 10^{10}°C/s [41]. It is believed that amorphous SiC phase forms at higher cooling rate than nanocrystalline structure and that the crystalline phase nucleates with the amorphous region while it is being cooled. However, another possibility is that melted or sublimated SiC reacted with oxygen to form $Si_xC_yO_z$ or SiO_2 which also has the tendency to form an amorphous phase.

B. Characterization of Diamond

Three different sizes of natural diamond powders (4-8, 10-15, and 20-25 μm) were used as starting materials. The high-temperature planar impact system (Figure 10(b)) was used for consolidation. The diamond samples were compacted at impact velocities of 1.2 and 1.9 km/s. The samples are well consolidated and the microhardness values of samples are in the range of 20-30 GPa. Diamond particles are very brittle and are subject to high bending moments due to their highly irregular shape. The number of cracks generated in the consolidated diamond powders tends to increase with an increase in the particle size of the starting diamond powders [1]. Generation of small amounts of graphite was detected by X-ray diffraction in the compacted 10-15 and 20-25 μm diamond powders. The transformation to graphite usually occurs in larger particle size specimens consolidated at room temperature. For larger particle size (10-25 μm), the interstitial void volume is larger than that of the small particle size (4-8 μm). Relative movement of constrained particles, upon densification, is greater for large particle size, which causes larger deformation per interstitial site. Therefore, larger interstitial void volumes will result in larger shock energy deposited at the powder surfaces and cause phase transformation. Furthermore, this transformation is also enhanced with the help of preheating. Scanning electron micrographs from

the interstitial melting areas of the compacted 20-25 μm diamond powders is shown in Figure 17. Small round diamond particles (0.5-1 μm) were observed in this sample. These small diamond particles are believed to be produced during the resolidification of the melting layer. Thicker surface layer (2-4 μm) were generated due to large particle size.

The recovered samples of compacted 4-8 μm diamond/C (15 wt%) and 4-8μm diamond/Si (7.5 wt%) mixture were also examined. Deformation of the softer component graphite decreases the pressure concentration and fills the pores between diamond particles. X-ray diffraction showed that part of the graphite powders was transformed to diamond. This is consistent with theoretical prediction [32] and results obtained by Potter and Ahrens [43]. These investigations showed, in room temperature experiments, that graphite transformed into diamond at pressures of 15-22 GPa. The consolidated diamond/C sample shows an extremely high microhardness value: >55 GPa. However, the recovered diamond/Si sample is not very well consolidated. We expected the heat generated from reaction between silicon and carbon to enhance the bonding, but the reaction did not occur. Furthermore, the addition of silicon will reduce the effective pressure transmitted to contact areas between diamond powders due to poor constraint. This resulted in poor consolidation.

C. Characterization of c-BN.

The recovered c-BN (10-20 and 40-50 μm) samples are very well consolidated. Figure 18 is a fracture surface of 10-20 μm c-BN which shows the melting of particle surfaces. This transgranular fractograph suggests that the bonding of the particle is excellent. The morphology of the c-BN is polyhedral. This particle geometry enhances the constraint between the particles during void collapse stage and results in larger energy deposition at the powder surfaces. Therefore, the microhardness value of the samples can reach 61 GPa. A highly angular particle shape would tend to decrease surface temperatures due to (1) poor constraint between particles and (2) generation of microcracks in the particle reducing the energy dissipation on the surface.

C-BN admixed with C (15 wt%) and a mixture of Ti (11 wt%) and C(9 wt%) was also consolidated. The graphite powders are severely deformed and uniformly distributed on the surfaces of the c-BN powder after shock consolidation. However, the cooling rate was not sufficiently high for the transformation of the graphite into diamond. The remaining graphite causes the degradation of the consolidated c-BN sample. Recovered c-BN admixed with Ti and C composite showed low microhardness value. The exothermic reaction of Ti and C did not take place during the passage of the shock wave. The remaining Ti and C caused the degradation of the sample.

4.2 Shock Consolidation Followed by Annealing or Hot Isostatic Pressing

Coker *et al.* [10] shock consolidated titanium alloys at room temperature and followed this treatment by HIP. This resulted in significant microstructural changes and improvement of

mechanical properties. Figure 19(a, b) shows typical microstructures after shock consolidation and hipping (Figure 19(c)). The Ti-6%Al-4%V alloy powder had a profuse dispersion of erbia and responded in a heterogeneous way to shock-wave passage. Whereas the interiors of the particles exhibited a lath structure (resulting from a martensitic phase transformation) with a high density of dislocations and deformation twins, the interparticle regions were characterized by a small grain size and a low dislocation density. The latter features are shown in Figure 19(b) and are the result of interparticle melting. Hot isostatic pressing annealed most of the dislocations; Figure 19(c) shows the resultant microstructure, with the characteristic erbia stringers. Hipping has, as a primary objective, the healing of the cracks that remain after the shock process. Figure 20 shows the yield stress and total elongation for shocked and shock + hipped titanium. The hip process enhanced the ductility of titanium considerably, while only decreasing the yield stress by approximately 10 pct. Conventionally forged material is also presented, for comparison purposes.

In an effort to eliminate cracking in Ti_3Al, elemental Ti and Al were added to the Ti_3Al powders and the mixture was shock consolidated. This work is described in detail by Shang and Meyers [7]. Annealing and hipping treatments were conducted subsequent to this; the objective of this treatment was to produce the reaction between Ti and Al powders. A double tube setup with low detonation velocity explosive was used. The shock pressure was calculated to be 9.5 GPa. Scanning electron microscopic analysis of recovered compacts after dynamic densification revealed that Ti and Al particles underwent a considerable amount of deformation and that the material was fully densified. The Ti_3Al particles seem to retain their initial sphericity. Well densified Ti_3Al+Ti+Al compacts were obtained (~95-98 % of the crystal density) and machined for subsequent hipping. Hot isostatic pressing (hipping) was conducted at 600°C and 1000°C for one hour. The shock densified Ti_3Al compacts were annealed to different temperatures ranging from 600 to 100°C. The unreacted regions (Ti + Al) and porosities were observed in specimens at different temperatures. These porosities were due to either (a) shrinkage that occurs when Ti and Al reacted; or (b) trapped gases causing expansion of voids. The density of Ti_3Al is 4.2 g/cm^3, while that of Ti and Al are 4.5 and 2.7 g/cm^3, respectively. Thus, the reaction leads to a 25% shrinkage. Since the capsules were not evacuated prior to shock densification, there is trapped air in them. Thus, when the reactants melt, the entrapped gases would expand and form spherical voids, which minimize the surface area. Consequently, hot isostatic pressing (HIP) was conducted at 600°C and 1000°C for one hour. SEM analysis of the material recovered from hipping at 600°C revealed that Ti and Al powders reacted with each other (Figure 21(a)). The dark regions correspond to the voids (marked in figure) and the grayish regions (marked in figure) correspond to the reaction products of Ti and Al. Analysis of the material recovered after hipping at 1000°C (Figure 21(b)) revealed that the reaction products bonded the Ti_3Al powders very well,

as compared to the compacts produced using hipping at 600°C. One can also see the phase separation in the interiors of the particles, after 1000°C HIP.

Compression tests also showed strong bonding between Ti_3Al powders after 1000°C hipping. These 1000°C-hipped specimens have an average ultimate compressive strength of 2 GPa and compressive fracture strain of 20%. In contrast, the average values of ultimate compressive strength and compressive fracture strain of dynamic-densified specimens are 1.4 GPa and 4.5%, respectively. Post-shock hipping can minimize the microcracks and tremendously increase the mechanical properties of the samples. Figure 22(a) and (b) shows the compressive property data for Ti_3Al alloys at room temperature. The data are from shock-densified specimens which were hipped or annealed at various temperatures. The data demonstrate that Ti_3Al exhibits an apparent increase in ductility with increasing temperature of annealing or hipping. The lower ultimate compressive stress and ductility of annealed specimens, compared to the 1000°C-hipped specimen, could be due to two reasons: (1) Ti and Al were not totally reacted in annealed specimens (2) shrinkage occurred when Ti and Al reacted, with the production of voids. Hipping at 600°C resulted in the α_2 (hcp) and orthorhombic structure and these structures exhibited a high yield stress but low ductility. The fracture surfaces from failed compressive specimens were observed by SEM. The specimen which was hipped at 600°C failed by a mixture of shear and axial splitting. Axial splitting (lower portion) is produced by tensile stresses at the tip of the pre-existing cracks and voids due to the compressive forces. Observation of the axial splitting region showed that the individual particles were heavily deformed and exhibited cleavage regions.

Figure 23 shows the reason for the enhanced ductility of the compact hipped to 1000°C. Phase separation occurs within the particles, and a crack is shown propagating through the two-phase region. Microcracks form and propagate through the brittle α_2 phase (dark) and are arrested or retarded by the B2 phase (light).

4.3 Reaction-assisted Shock Consolidation

The use of shock-induced chemical reactions to help the consolidation of ceramic powders was pioneered by Sawaoka and Akashi [44] and is described in their patent. Elemental powder mixtures (e.g., Ti and C) are added to the ceramic (e.g., BN) powder. The shock wave triggers the highly exothermic Ti + C reaction, which produces the ceramic TiC and at the same time releases a great amount of heat. This heat helps to "soften" the BN surfaces and has been found to be instrumental in the bonding process. Figure 24 shows the process schematically. Yu, Meyers, and Thadhani [13] and Yu and Meyers [43] applied this concept to aluminides and silicides, respectively. Their results are presented in the two sections that follow, in an abbreviated form.

A. Chemically-assisted shock consolidation of TiAl [13]

The hard and brittle TiAl powders are difficult to shock consolidate without additives. Thus, Nb and Al powders were added to TiAl powders with the intent of initiating a shock-induced

reaction to generate heat and produce an intermetallic compound binder phase to assist in the consolidation of TiAl. Figure 25 shows the cross section of a sample containing TiAl, Nb, and Al, shocked at 2.3 km/s impact velocity. It is clearly seen that the bottom portion of the capsule underwent better bonding. This corresponds to the region of higher mean bulk temperature. The profile of the well consolidated region is clearly evident.

Figure 26, at higher magnification, shows the optical micrograph of a region near the top of the cross section. It is clearly seen that Nb powders just surround TiAl powders; they did not react with Al powders. Figure 26(b) shows the quantitative analysis of Figure 26(a) by SEM. There is no reaction between Nb and TiAl powders. At the central region of the cross section, reaction took place with residual Nb particles remaining. Figure 26(c) (bottom part of cross section) shows that Nb and Al powders reacted with each other and with TiAl powders. The reaction products bonded the TiAl powders together. Figure 26(d) shows that all points in this region (O, P, Q, R) were reaction products which had almost the same composition.

It is interesting to notice that reaction does not take place as postulated in Figure 24, but in a more complex mode, with involvement of the inert intermetallic compound and binders. This aluminum was found to react with the TiAl powder. They are thought to be due to a Ti-Al-Nb ternary compound. These results clearly show that chemically-induced bonding is a concept that can be applied to assist in consolidation of metallic systems.

B. Chemically-assisted Shock Consolidation of Silicides [43]

Different quantities of reactants (niobium and silicon powders) mixed in $NbSi_2$ stoichiometry were added to $NbSi_2$ powders: 10, 30, and 50 wt%. The micrographs of the cross-sections of recovered compacts are shown in Figures 27-29. In Figure 27, the composition of the specimen was Nb-Si (10 wt %) and $NbSi_2$ (90 wt %), and most of the areas show that Nb-Si-$NbSi_2$ powders remained unreacted; however, the powders were well compacted. In this case, the silicon powder underwent large plastic deformation, surrounding the niobium and $NbSi_2$ powders, but the shock pressure and temperature were not sufficient to initiate the chemical reactions between reactant materials. As the quantity of Nb-Si powders was increased, the extent of the chemical reaction was also observed to increase. In the specimen containing 30 wt% Nb-Si powders, two different regions were observed and are shown in Figure 28. The top portion corresponds to the unreacted region, and the bottom portion reveals fully reacted region, in accordance with the maximum temperature profiles. Figures 28(b) and 28(c) show a scanning electron micrograph and composition maps for silicon and niobium. It is clear that no reaction occurred; this represents the top portion of the capsule. The morphology of the reacted region is quite different and the profuse presence of voids is noteworthy. Compositional mapping (not shown) demonstrated that reaction between niobium and silicon took place. As the quantity of the Nb-Si powders was increased to 50 wt% (Figure 29), most areas showed full reaction and an

appearance similar to that of 100% elemental powders. The higher magnification micrograph of the specimen containing 50 wt% Nb-Si powder mixture is shown in Figure 29(b) and (c). The dot mapping shows that the composition is uniform (except for voids). From these results, it seems that both the quantity of Nb-Si powders and shock parameters have a considerable effect on the synthesis process.

The void concentrations in the reacted regions were 9%, 24% and 30% for 10% Nb + Si, 30%, and 50% addition, as shown in the plot in Figure 30. The increase in the number of voids with increased proportion of reactants indicates that more shrinkage and gas evolution occurred due to the heat generated by the exothermic reaction of Nb-Si powders. This shows that the degree of reaction depends on pressure, temperature, and the fraction of reactant materials.

The preliminary results obtained on chemically-assisted shock consolidation indicate that reactions can be helpful in shock consolidation. Careful control and optimization of experimental conditions and materials systems is necessary for successfully obtaining good compacts. Very encouraging results have recently been obtained by Potter and Ahrens [6, 42], Tan and Ahrens [5], and Ahrens *et al.* [32] by the addition of graphite, Si, SiC, and Si_3N_4 to diamond or boron nitride powders. It is felt by the co-authors that this area requires concentrated and intensive research.

5. Conclusions

It is very difficult to shock consolidate hard materials (intermetallic compounds and ceramics) because of two reasons:

(a) high shock pressures are required to generate sufficient energy for bonding of the powders

(b) the fracture toughness of these hard materials is such that they are very flaw-sensitive.

Thus, small flaws invariably present after shock densification are easily activated by tensile reflected stress or thermo-mechanical stresses during cooling (residual due to temperature gradients). Figure 11 shows the shock stresses required for consolidation as well as critical stresses for activation of flaws. It is clear that ceramics and intermetallics are in the "danger zone", arbitrarily set for a tensile stress equal to 10% of the compressive shock stress.

Ongoing research efforts aimed at circumventing this major problem are described. The basic approach is to provide energy to the material through means complementary to the shock energy. Three different approaches have been implemented, with varying degrees of success:

1 - Use of local shock-induced reactions to increase temperatures of particle interfaces and enhance bonding.

2 - Shock densification at a low pressure (just above threshold for pore collapse) followed by hot isostatic pressing or sintering.

3 - Shock consolidation of pre-heated specimens.

These approaches have been applied to a number of metals, intermetallic compounds, and ceramics. In combination with optimized fixture designs, they could lead to crack-free compacts of simple shapes (disks and cylinders).

Acknowledgements

The research described herein has been supported, over the 1988-1992 period, by National Science Foundation Grants DMR 8713258 and DMR 91-5835R1. We also thank McDonnell-Douglas, General Electric, the State of New Mexico (through the Center for Explosives Technology Research, in Socorro, New Mexico), and United Technologies Government Products Division for support prior to that period. The help of N. N. Thadhani, Georgia Institute of Technology, has been invaluable. The work described here has been carried out in collaboration with N. N. Thadhani, A. Szecket, L. H. Yu, A. Ferreira, S. L. Wang, and S. N. Chang. We benefitted immensely from numerous discussions, over the past eight years, with Professor A. Sawaoka, Tokyo Institute of Technology, and Dr. R. A. Graham, Sandia National Laboratories.

The research described here and in the papers cited in the references would not have been possible without the dedicated support of engineers and technicians of the TERA (Terminal Effects Research and Analysis) and CETR (Center for Explosives Technology Research) groups at New Mexico Tech.

References

1. T. Akashi and A. B. Sawaoka: *J. Mater. Sci.*, 1987 , vol. 22, pp. 3276-86.
2. T. Akashi and A. B. Sawaoka: *J. Mater. Sci.*, 1987 , vol. 22, p. 1127.
3. S. Sawai and K. Kondo: *J. Am. Ceram. Soc.*, 1990 , vol. 73, pp. 2428-34.
4. S. Sawai and K. Kondo: *J. Am. Ceram. Soc.*, 1988 , vol. 71, p. C-185.
5. H. Tan and T. J. Ahrens: *J. Mater. Res.*, 1988 , vol. 3, pp. 1010-20.
6. D.K. Potter and T.J. Ahrens: *Appl. Phys. Lett.*, 1987 , vol. 51, p 317.
7. S. S. Shang and M. A. Meyers: *Metall. Trans.*, 1991 , vol. 22A, pp. 2667-76.
8. S. S. Shang, K. Hokamoto and M. A. Meyers: *J. Mater. Sci.*, 1992, in press.
9. S. L. Wang, M. A. Meyers and A. Szecket: *J. Mater. Sci.*, 1988 , vol. 23, pp. 1786-1804.
10. H. L. Coker, M. A. Meyers and J. F. Wessels: *J. Mater. Sci.*, 1991, vol. 25, p. 1277.
11. A. Ferreira, M. A. Meyers, N. N. Thadhani, S. N. Chang and J. R. Kough: *Metall. Trans.*, 1991 , vol. 22A, pp. 685-95.
12. A. Ferreira, M. A. Meyers, N. N. Thadhani: *Metall. Trans.*, 1992, in press.
13. L. H. Yu, M. A. Meyers and N. N. Thadhani: *J. Mater. Res.*, 1990, vol. 5, p. 302.
14. W. H. Gourdin: *J. Appl. Phys.*, 1984, vol. 55, p. 172.
15. R. B. Schwarz, P. Kasiraj, T. Vreeland Jr and T. J. Ahrens: *Acta Metall.*, 1984, vol. 32, p. 1243.
16. V. F. Nesterenko, Proc. Novosibirsk-Conference on Dynamic Compaction, 1988, p. 100.
17. M. A. Meyers and L. E. Murr: in *Shock Wave and High - Strain - Rate Phenomena in Metals*, eds. M.A. Meyers and L.E. Murr, Plenum Press, N.Y., 1981, p. 487.
18. V. F. Lotrich, T. Akashi and A. Sawaoka : in *Metallurgical Applications of Shock Wave and High - Strain - Rate Phenomena*, eds. L.E. Murr, K.P. Staudhammer and M.A. Meyers, Marcel Dekker Inc., N.Y., 1986, p. 277.
19. N. E. Elliott and K. P. Staudhammer: in *Metallurgical Applications of Shock Wave and High - Strain - Rate Phenomena*, eds. M. A. Meyers, L. E. Murr and K. P. Staudhammer, Marcel Dekker Inc., N.Y., 1992, pp. 371-381.
20. A. Ferreira and M. A. Meyers: in *Metallurgical Applications of Shock Wave and High - Strain - Rate Phenomena*, eds. M. A. Meyers, L. E. Murr and K. P. Staudhammer, Marcel Dekker Inc., N.Y., 1992, p. 361.
21. M. M. Carroll and A. C. Holt: *J. Appl. Phys.*, 1972, vol. 43, p. 1626.
22. F. R. Norwood and R. A. Graham: in *Metallurgical Applications of Shock Wave and High - Strain - Rate Phenomena*, eds. M. A. Meyers, L. E. Murr and K. P. Staudhammer, Marcel Dekker Inc., N.Y., 1992, p. 989.
23. S. S. Shang and M. A. Meyers: unpublished results.
24. A. S. Helle, K. E. Easterling and M. F. Ashby: *Acta Metall.*, 1985, vol. 33, pp. 2163-2174.

25. H. F. Fischmeister and E. Arzt: *Powder Metall.*, 1983, vol. 26, p. 82.
26. E. Arzt: *Acta Metall.*, 1982, vol. 30, p. 1883.
27. K.P. Staudhammer and L.E. Murr: in *Shock Waves for Industrial Applications*, ed. L.E. Murr, NOYES Publishers, N.J., 1988, p. 237.
28. F. R. Norwood, R. A. Graham and A. Sawaoka: in *Shock Waves in Condensed Matter*, ed. Y. M. Gupta, Plenum Press, 1986, p. 837.
29. N. N. Thadhani, G. T. Holman, B. Romero and R. A. Graham: CETR Report No. A-01-91, 1991.
30. G.E. Korth, J.E. Flinn and R.C. Green: in *Metallurgical Applications of Shock Wave and High - Strain - Rate Phenomena*, eds. L.E. Murr, K.P. Staudhammer and M.A. Meyers, Marcel Dekker Inc., N.Y., 1986, p. 129.
31. A. H. Mutz and T. Vreeland, Jr.: in *Metallurgical Applications of Shock Wave and High - Strain - Rate Phenomena*, eds. M. A. Meyers, L. E. Murr and K. P. Staudhammer, Marcel Dekker Inc., N.Y., 1992, p. 425.
32. T. J. Ahrens, G. M. Bond, W. Yang and G. Liu: in *Metallurgical Applications of Shock Wave and High - Strain - Rate Phenomena*, eds. M. A. Meyers, L. E. Murr and K. P. Staudhammer, Marcel Dekker Inc., N.Y., 1992, p. 339.
33. A. B. Sawaoka and Y. Horie: in *Metallurgical Applications of Shock Wave and High - Strain - Rate Phenomena*, eds. M. A. Meyers, L. E. Murr and K. P. Staudhammer, Marcel Dekker Inc., N.Y., 1992, p. 323.
34. R. Prummer: *Explosivverdichtung Pulvriger Substanzen* , Springer-Verlag, Berlin, Germany, 1987.
35. M. A. Meyers, B. B. Gupta and L. E. Murr: *J. of Metals*, 1981, vol. 33, p. 21.
36. M. A. Meyers and S. L. Wang: *Acta Metall.*, 1988, vol. 4, pp. 925-36.
37. R. K. Gurney: *The Initial Velocities of Fragments From Bombs, Shells, and Grenades*, BRL Report 405, 1943.
38. L. H. Yu and M. A. Meyers: in *Metallurgical Applications of Shock Wave and High - Strain - Rate Phenomena*, eds. M. A. Meyers, L. E. Murr and K. P. Staudhammer, Marcel Dekker Inc., N.Y., 1992, p. 303.
39. M. A. Meyers and H.-r. Pak: *J. Mater. Sci.*, 1985, vol. 20, p. 2133.
40. S. L. Wang, M. A. Meyers and R. A Graham: in *Shock Waves in Condensed Matter*, ed. Y. M. Gupta, Plenum Press, 1986, p. 731.
41. D. G. Morris: *Met. Sci.*, 1981 , vol. 15, p. 116.
42. D. K. Potter and T. J. Ahrens: *J. Appl. Phys.*, 1988, vol. 63, p. 910.
43. L. H. Yu and M. A. Meyers: *J. Mater. Sci.*, 1991, vol. 26, p. 601.

44. K. Kunishige, Y. Horie and A. B. Sawaoka: in *Metallurgical Applications of Shock Wave and High - Strain - Rate Phenomena*, eds. M. A. Meyers, L. E. Murr and K. P. Staudhammer, Marcel Dekker Inc., N.Y., 1992, p.353.

List of Figures

Figure 16. Transmission electron micrograph of consolidated 325 mesh SiC showing (a) lattice distortion in the interior of SiC particle and (b) the surface layer in the interparticle region.

Figure 17. Scanning electron micrograph of the melting layer after the resolidification from 20-25 μm diamond.

Figure 18. Scanning electron micrograph of fracture surface from consolidated 10-20 μm c-BN.

Figure 19. Transmission electron micrograph showing (a) and (b) as-shocked and (c) shocked + hipped microstructure in a titanium alloy (from Coker *et al.* [10]).

Figure 20. (a) Yield stress and (b) elongation of commercial purity titanium conventionally forged and shock (comp.) processed as a function of temperature (from Coker *et al.* [10]).

Figure 21. Scanning electron micrograph from shock-densified Ti_3Al+Ti+Al alloys (a) hipped at 600°C; (b) hipped at 1000°C at 1000°C in which the different regions were identified by EDS analysis (from Shang and Meyers[7]).

Figure 22. Compressive properties of Ti_3Al hipped or annealed from 600°C to 1000°C (a) yield strength, ultimate compressive strength, and fracture strength; (b) maximum compressive fracture strain (from Shang and Meyers[7]).

Figure 23. Scanning electron micrograph showing intergranular and transgranular cracks in the interior of Ti_3Al particle; white particles are ductile phase and dark particles are brittle phase. Arrow shows how cracks are arrested by ductile phase (from Shang and Meyers [7]).

Figure 24. Sequence of events in chemically-assisted shock consolidation.

Figure 25. Typical cross-section of a shocked compact containing elemental powder reactants; notice bottom part (reacted) and top part (unreacted) (from Yu, Meyers, and Thadhani [13]).

Figure 26. (a) Optical micrograph of the top region of capsule containing TiAl + Nb + Al; (b) quantitative analysis of (a).

Figure 26. (continued): (c) Optical micrograph of the bottom region of capsule; (d) quantitative analysis of (c) (from Yu, Meyers, and Thadhani [13]).

Figure 27. (a) Optical micrograph of cross-section of compact (Nb 6.2 wt%, Si 19 3.84 wt%, $NbSi_2$ 90 wt%. (b) Scanning electron micrograph of local region in (a). (c) Scanning electron micrograph of void of (a) (from Yu and Meyers [43]).

Figure 28. (a) Optical micrograph of cross-section of compact (Nb 18.6 wt%, Si 11.4 wt%, $NbSi_2$ 70 wt%). (b) Scanning electron micrograph of unreacted region, silicon dot mapping. (c) Niobium do mapping. ((d) Scanning electron micrograph of reacted region.) (From Yu and Meyers [43].)

Figure 29. (a) Optical micrograph of cross-section of compact (Nb 31 wt%, Si 19 wt%, $NbSi_2$ 50 wt%). (b) Scanning electron micrograph of unreacted region, silicon dot mapping. (c) Niobium do mapping. ((d) Scanning electron micrograph of reacted region.) (From Yu and Meyers [43].)

Figure 30. Void concentration plotted against Nb-Si weight percentage. (From Yu and Meyers [43].)

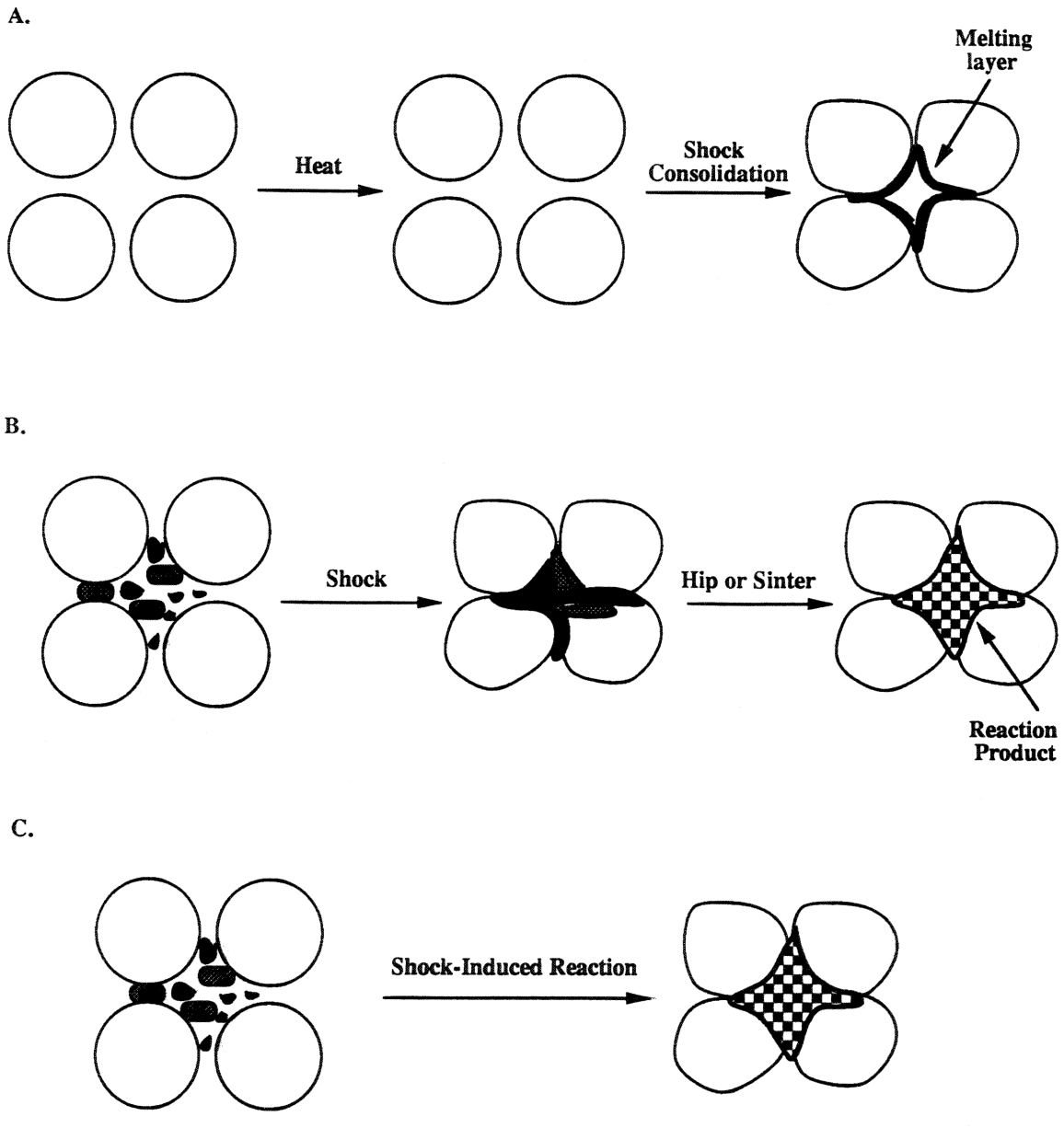

Figure 1. Schematic representation of three approaches used to improve performance of shock consolidation and minimize cracking; (a) pre-heating of powders; (b) post-shock hip or sinter processing; (c) use of shock-induced reaction to assist bonding.

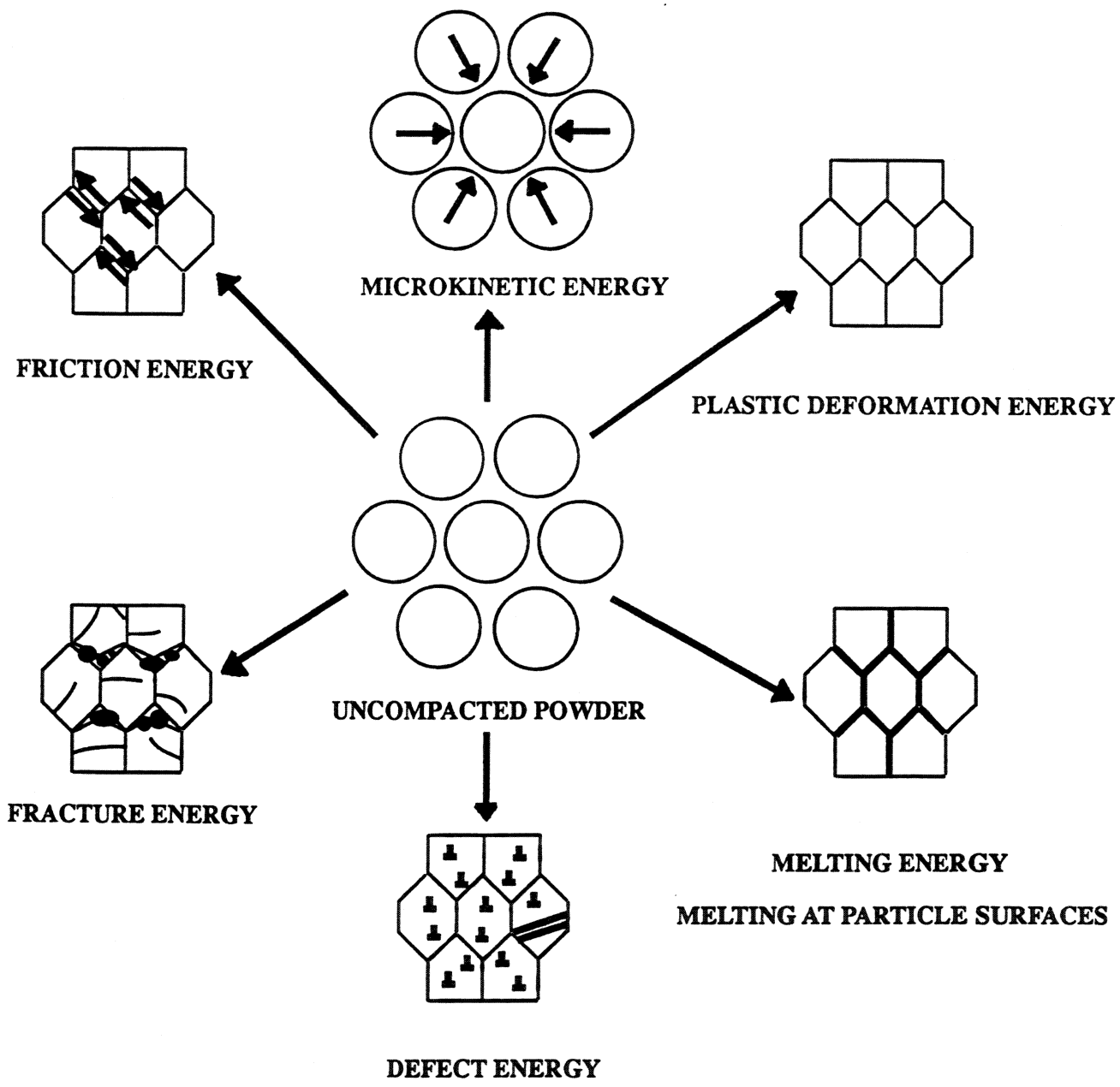

Figure 2. Various modes of energy dissipation in shock compression of powders.

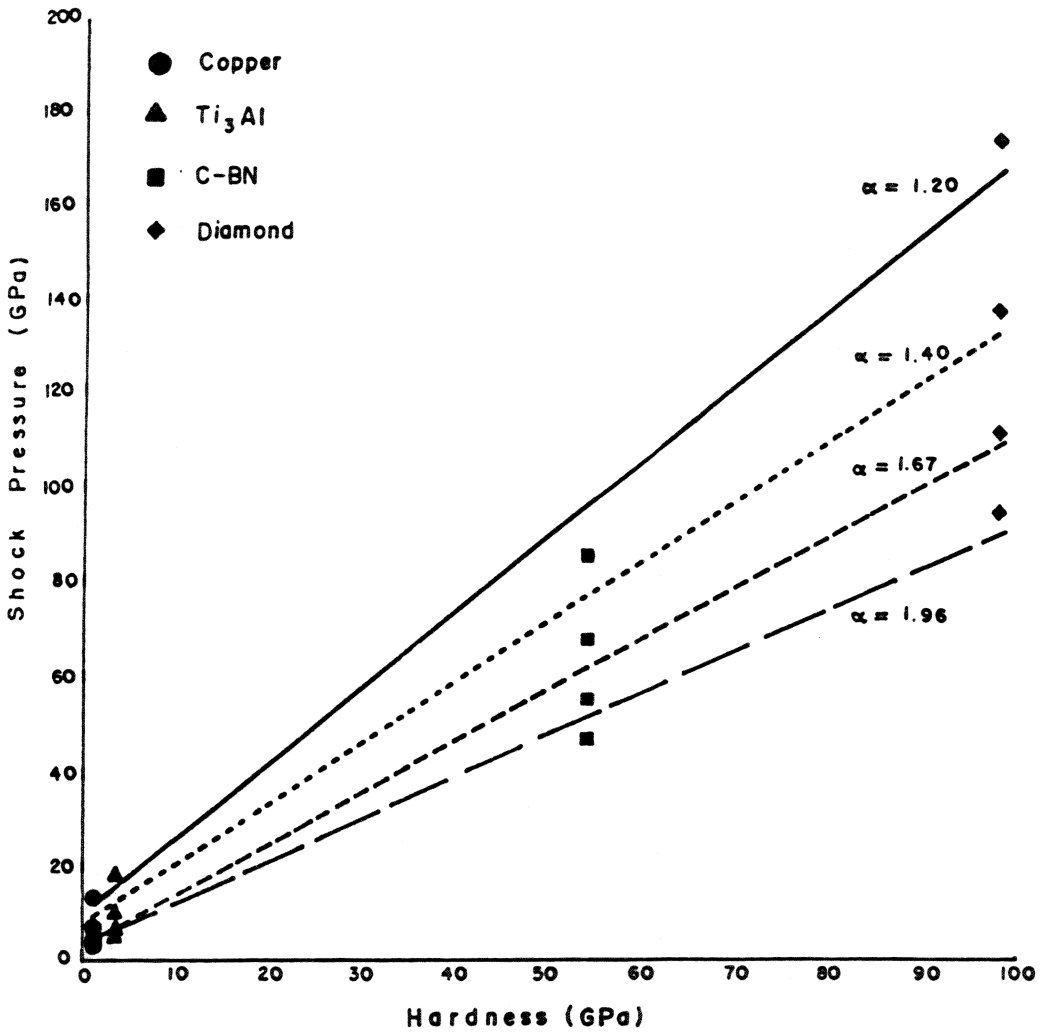

Figure 3. Pressure required for shock consolidation vs hardness at several distentions (from Ferreira and Meyers [20]).

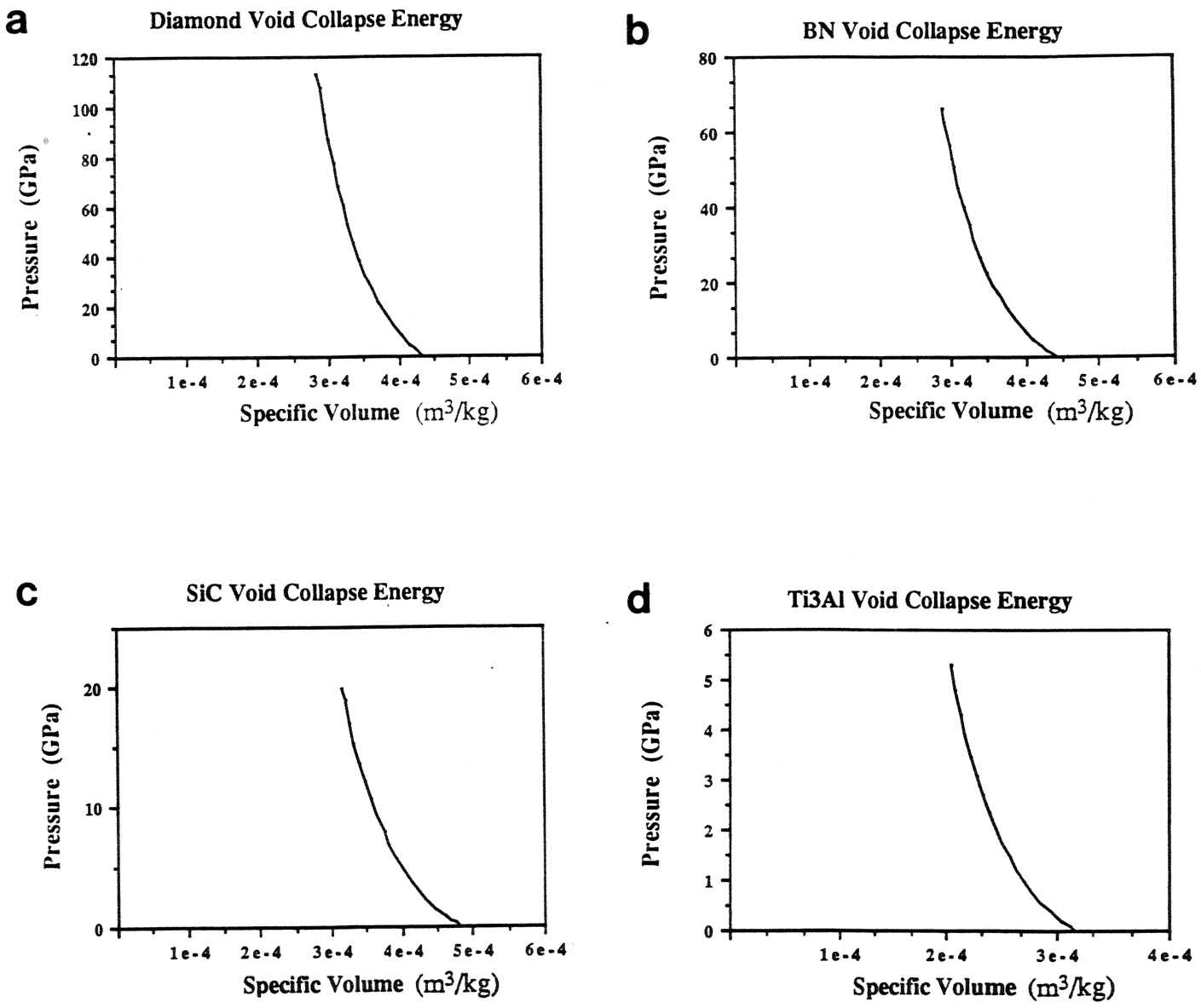

Figure 4. The external pressure vs specific volume for diamond, c-BN, SiC and Ti_3Al during the plastic yielding stage, according to Helle *et al.*'s [24] model.

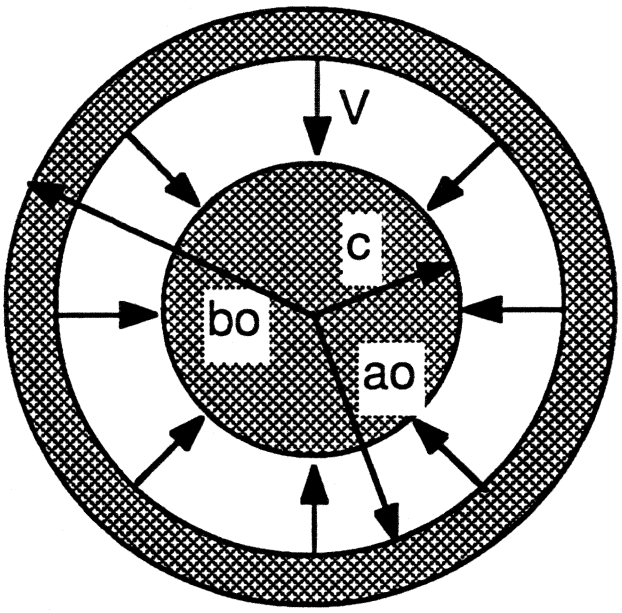

Figure 5. Carroll-Holt [21] sphere collapse configuration modified by Nesterenko [16] to incorporate micromechanical energy and particle size.

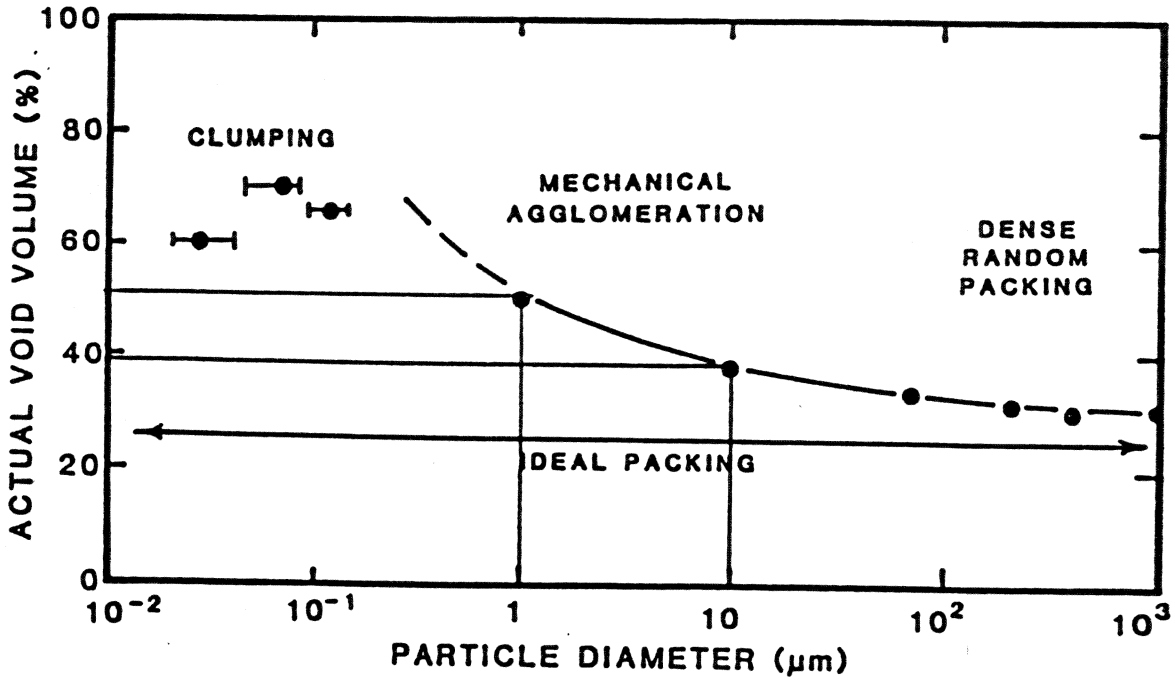

Figure 6. Particle diameter vs. void volume for monosize powders (from Staudhammer and Murr [27]).

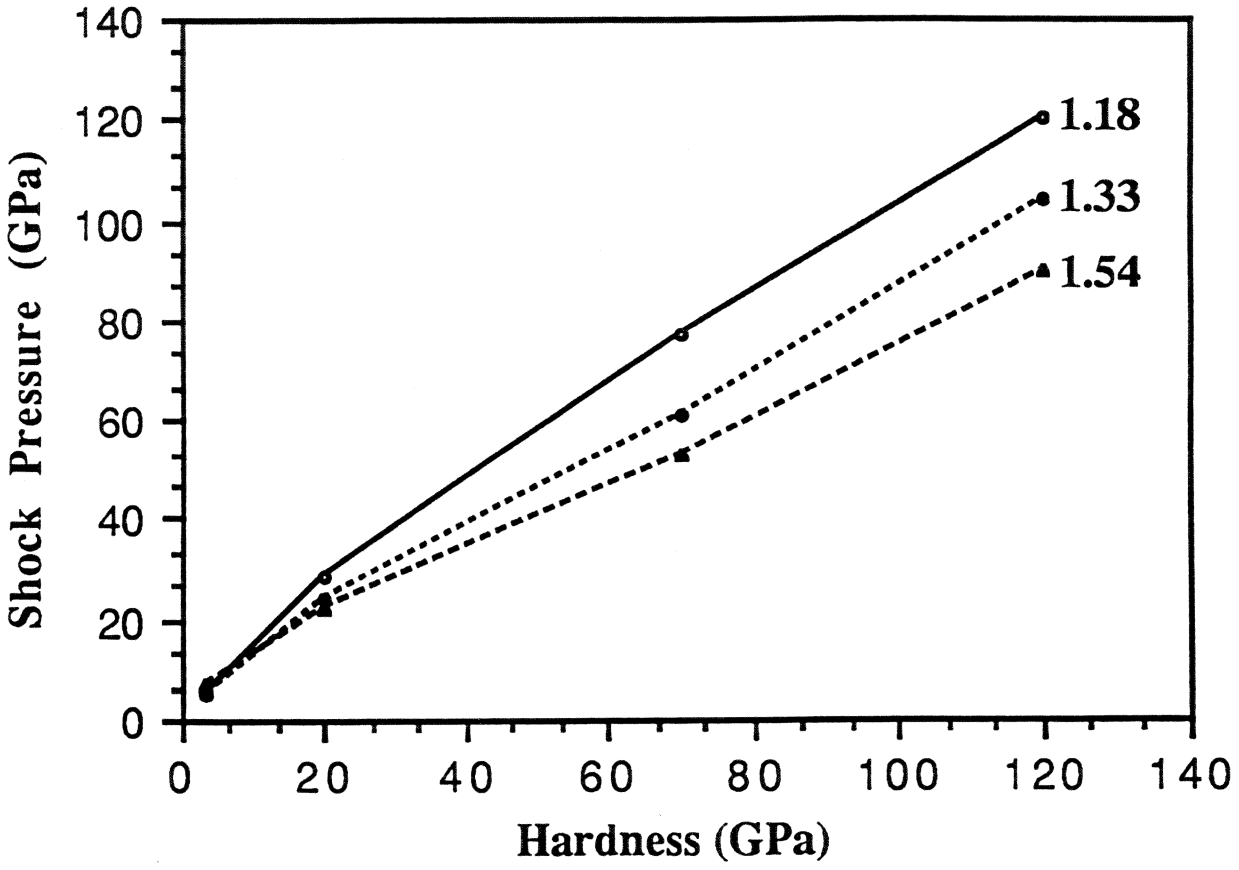

Figure 7. Pressure required for shock consolidation vs. hardness for three distentions (1.18, 1.33, and 1.54), according to improved model (from Shang and Meyers [23]).

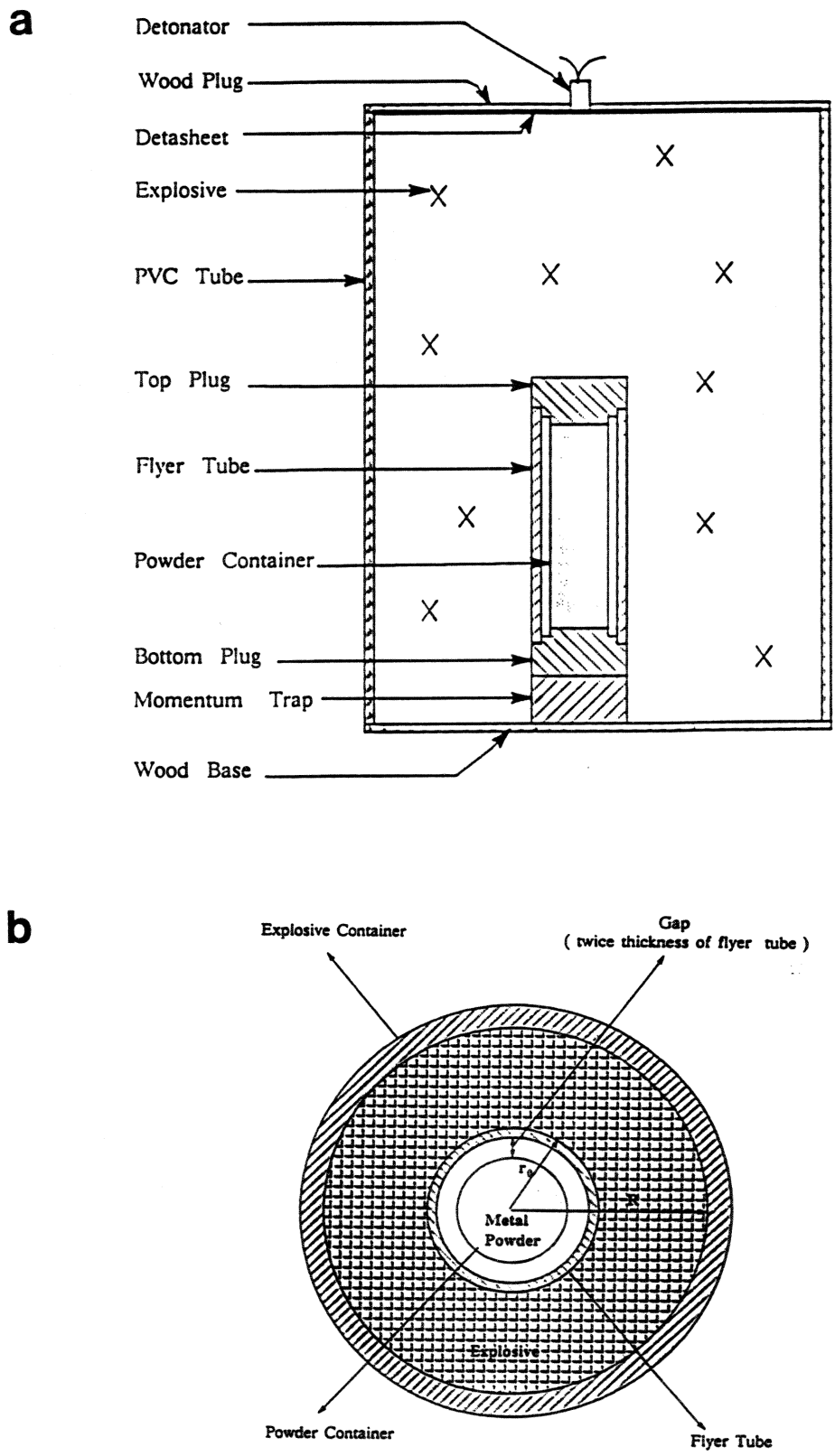

Figure 8. (a) Cylindrical shock consolidation system using flyer tube; (b) cross-section of system (from Meyers and Wang [36]).

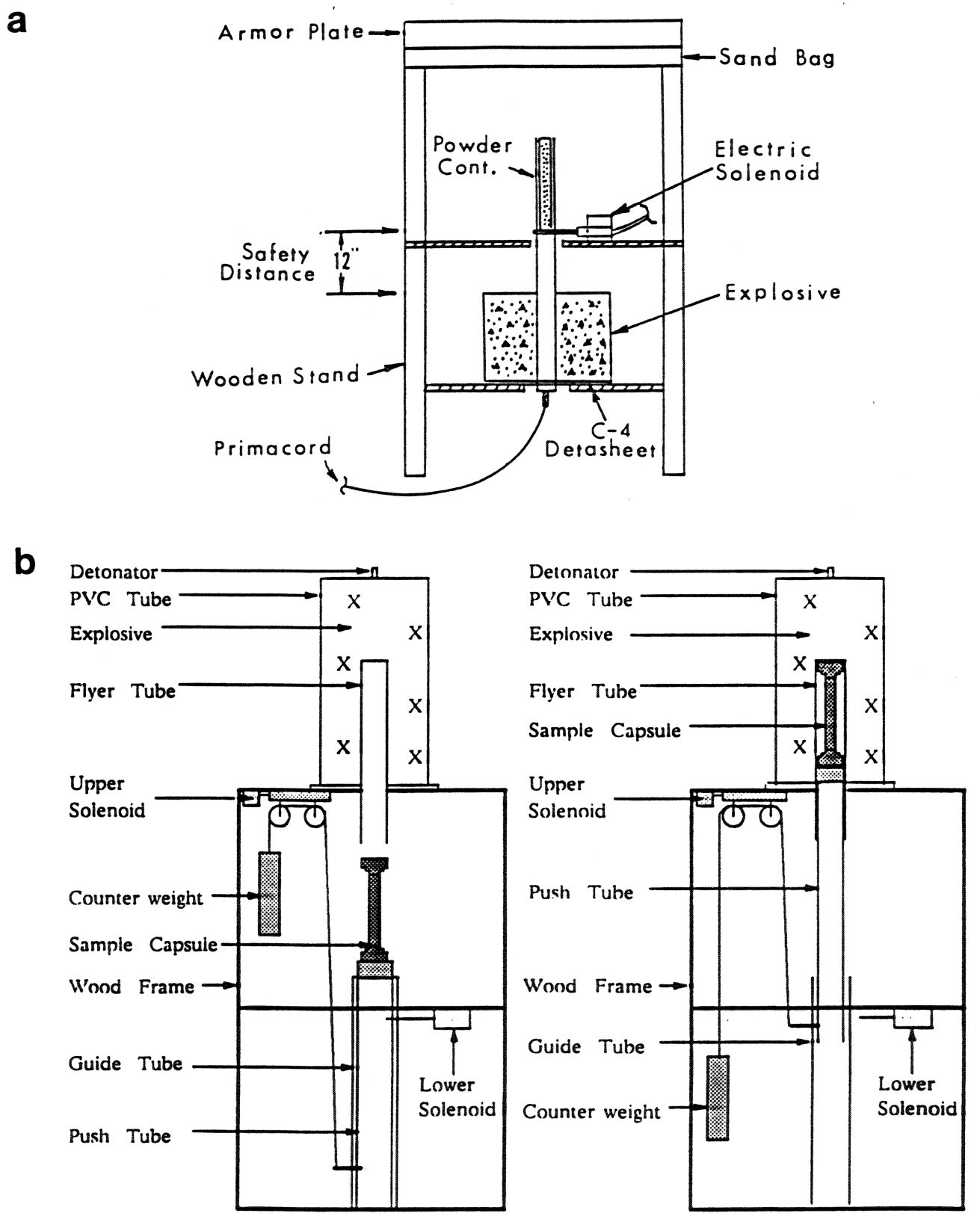

Figure 9. High temperature cylindrical shock consolidated systems: (a) system used by Wang, Meyers, and Szecket [9]; (b) system used by Ferreira *et al.* [11].

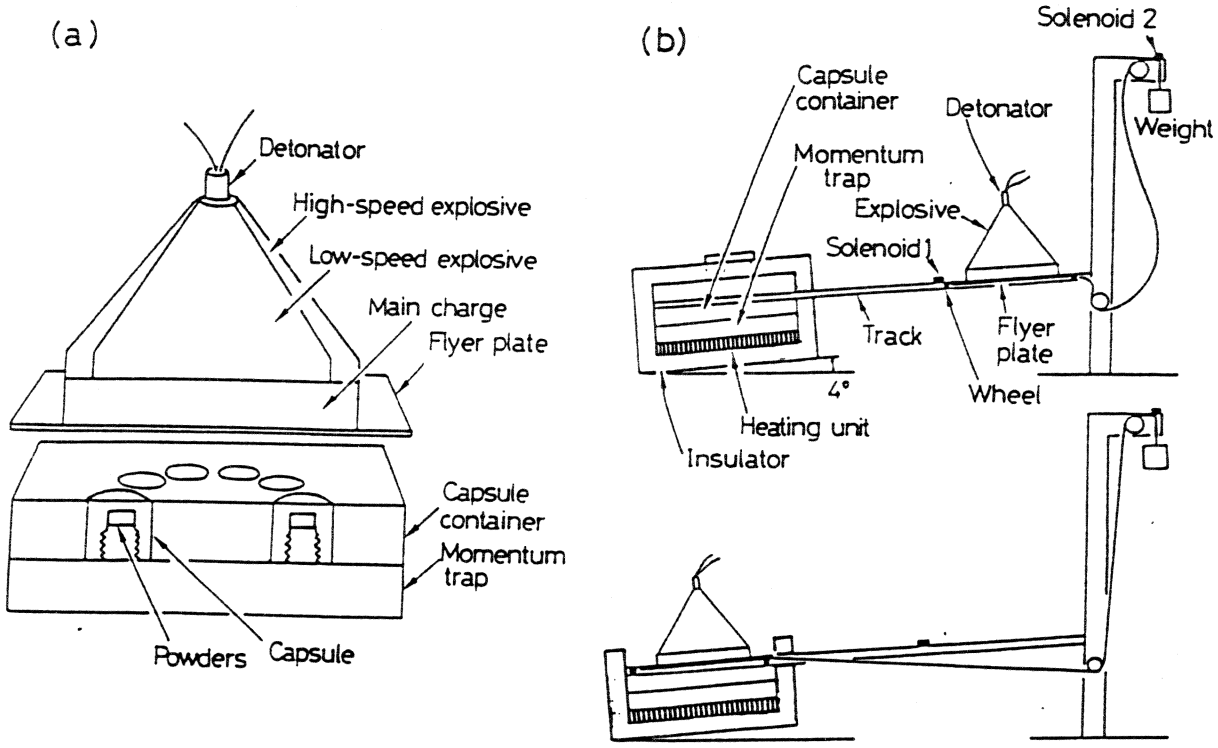

Figure 10. Sawaoka planar shock consolidation system; (a) section of system showing flyer plate acceleration setup with explosive lens and cross-section of capsules and tooling; (b) high-temperature adaptation of system (from Yu and Meyers [38]).

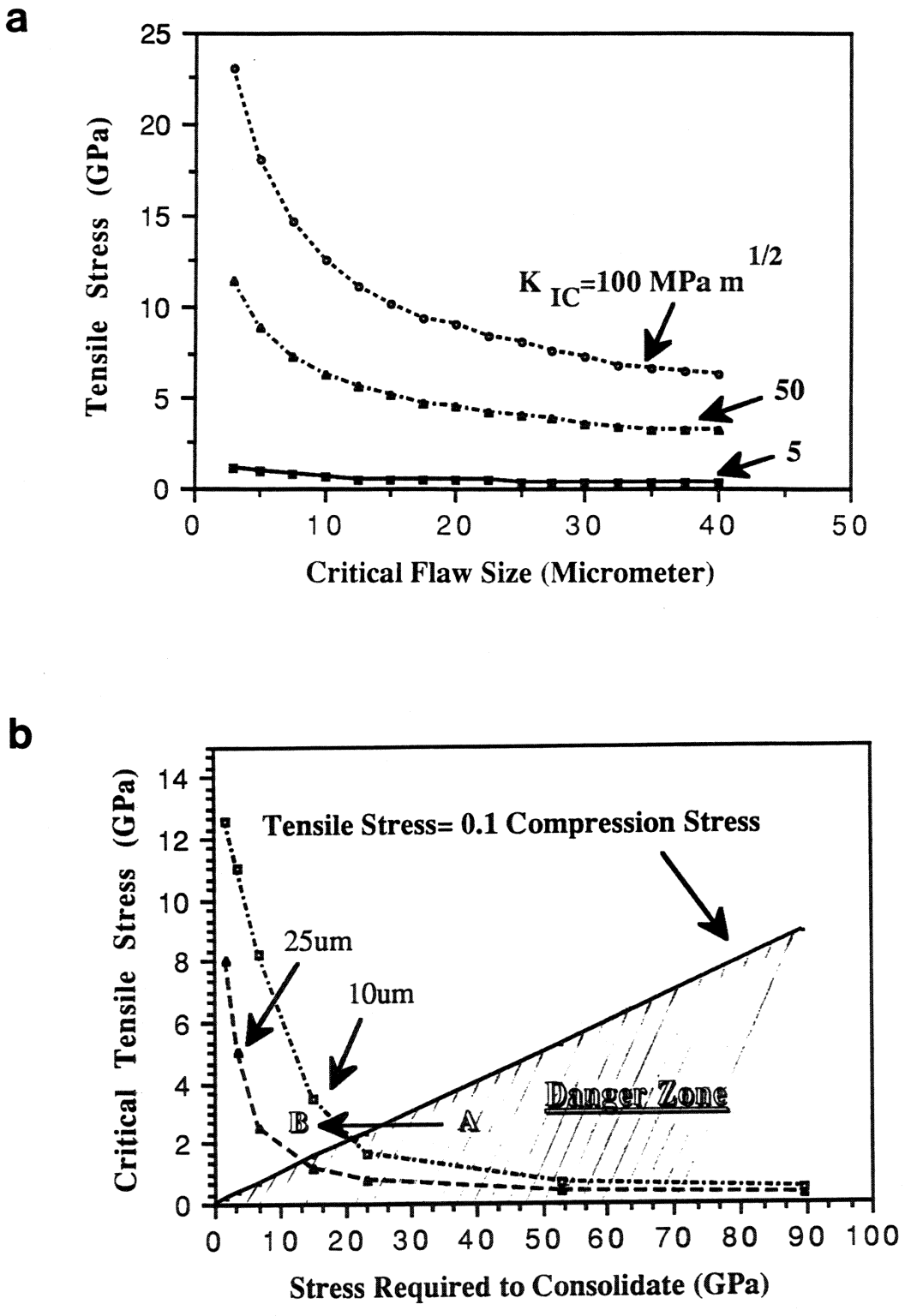

Figure 11. (a) Critical flaw size as a function of tensile stress for materials with different fracture toughnesses; (b) variation of critical tensile stress for 10 and 25 μm flaw activation with shock stress required for consolidation: notice danger zone.

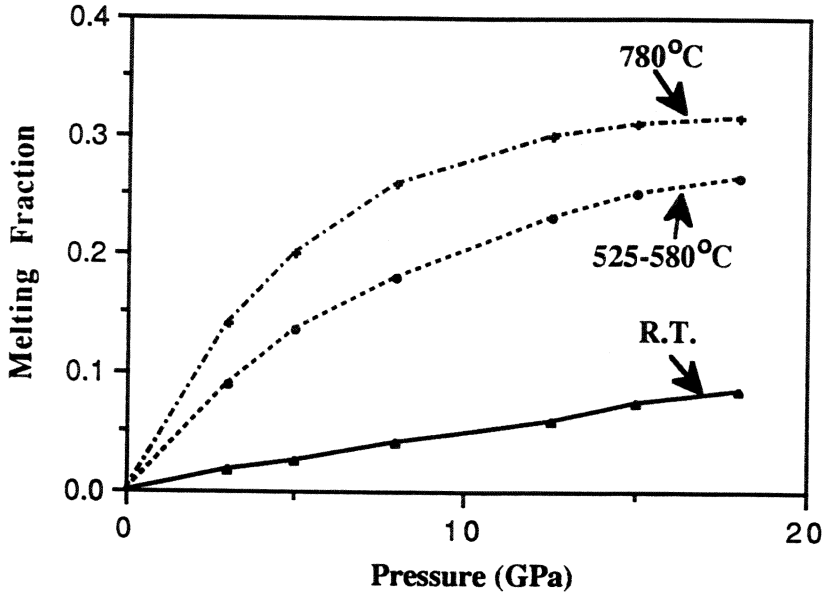

Figure 12. Shock-induced melting (as a fraction of total volume) as a function of shock pressure for IN718 superalloy powder at three different temperatures (from Wang, Meyers, and Szecket [9]).

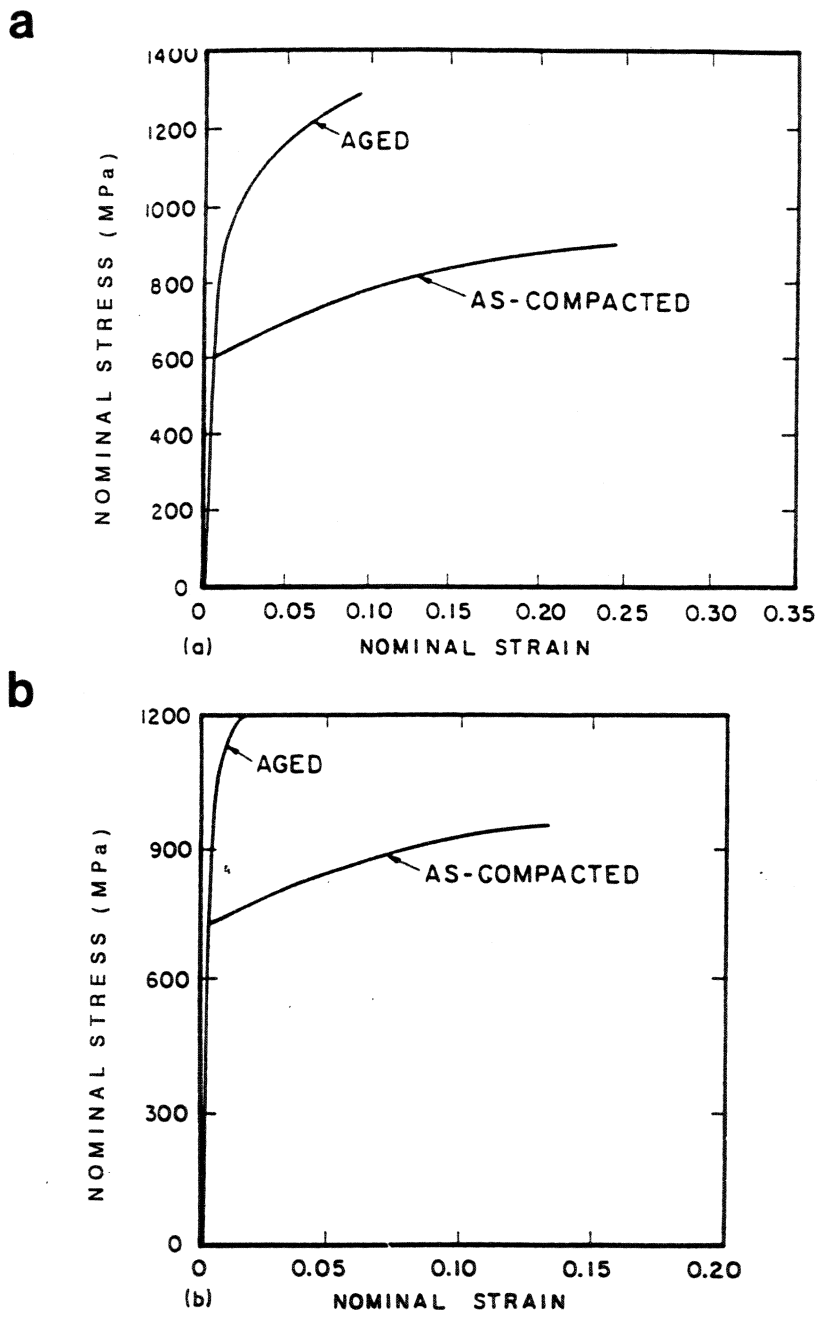

Figure 13. Tensile stress-strain response of IN718 powders shock consolidated at (a) 740°C and (b) 525°C in the as-consolidated and consolidated plus aged conditions (from Wang, Meyers, and Szeckett [9]).

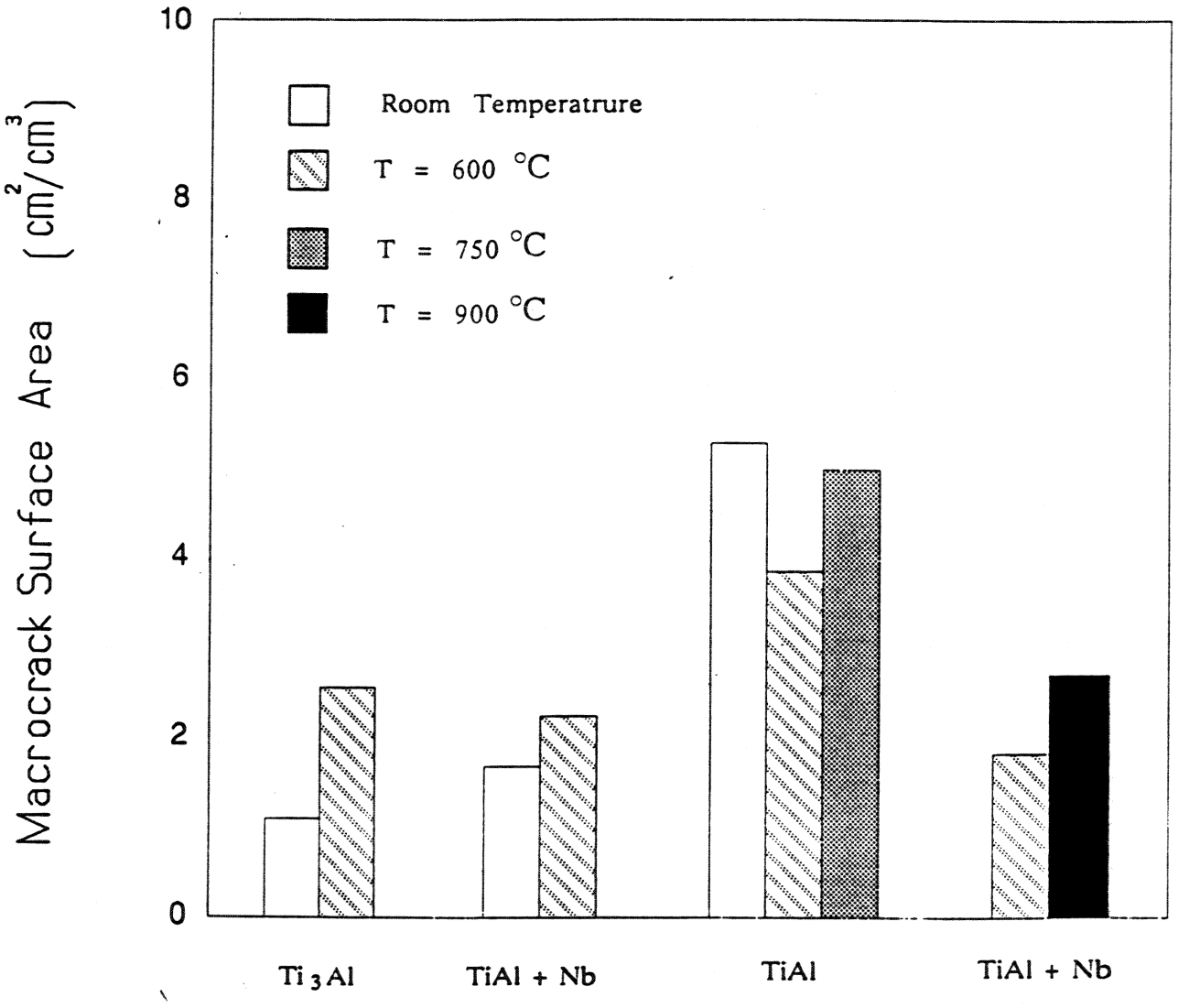

Figure 14. Effect of initial temperature on the average crack density of compacts (from Ferreira *et al.* [11]).

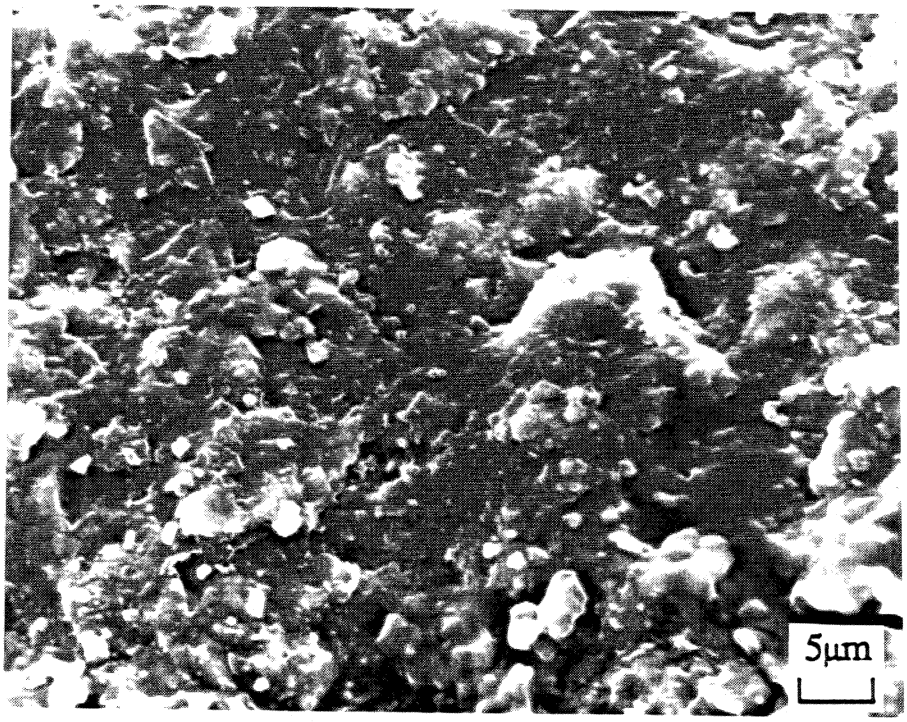

Figure 15. Scanning electron micrograph of fracture surface of consolidated 7 μm SiC.

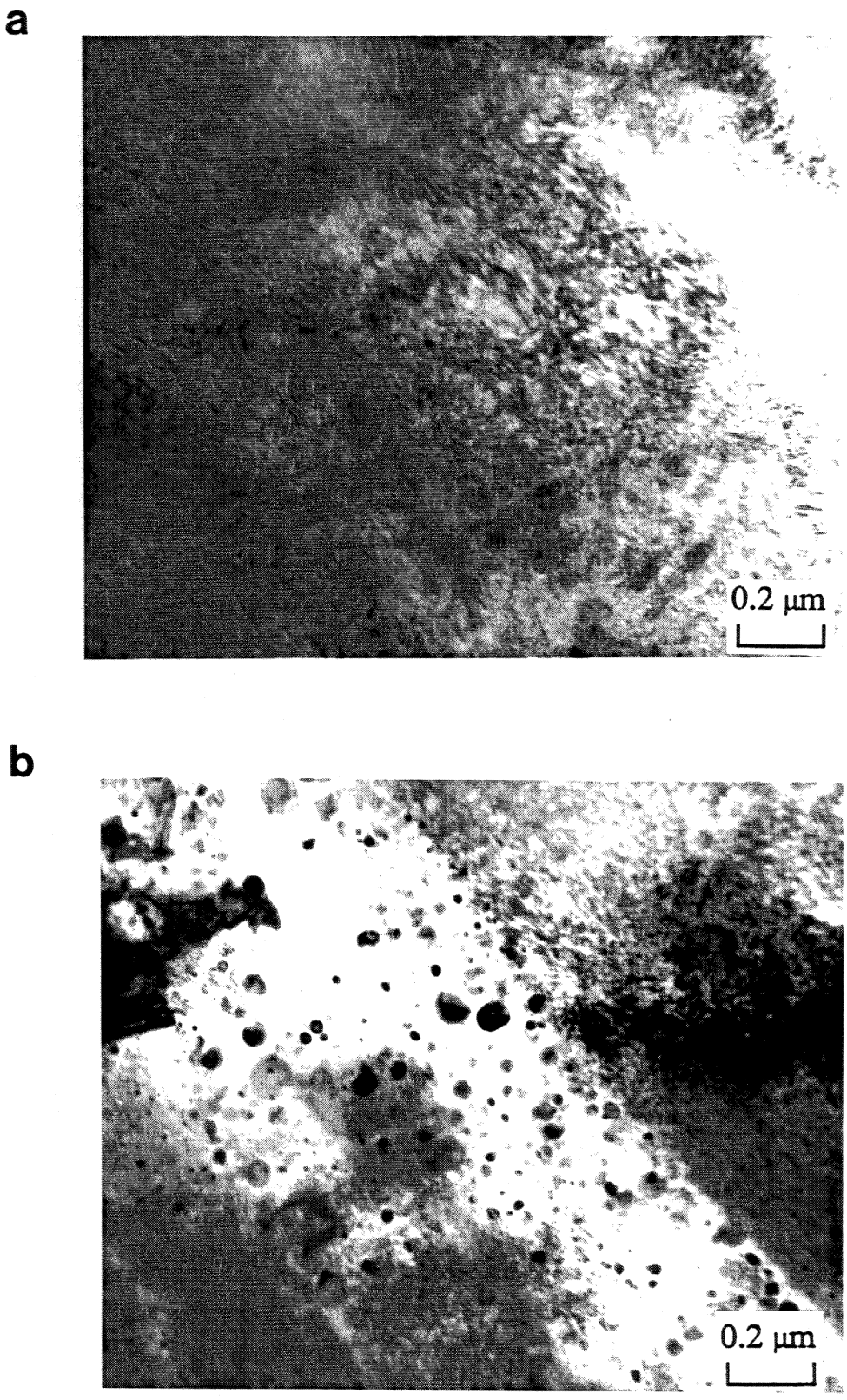

Figure 16. Transmission electron micrograph of consolidated 325 mesh SiC showing (a) lattice distortion in the interior of SiC particle and (b) the surface layer in the interparticle region.

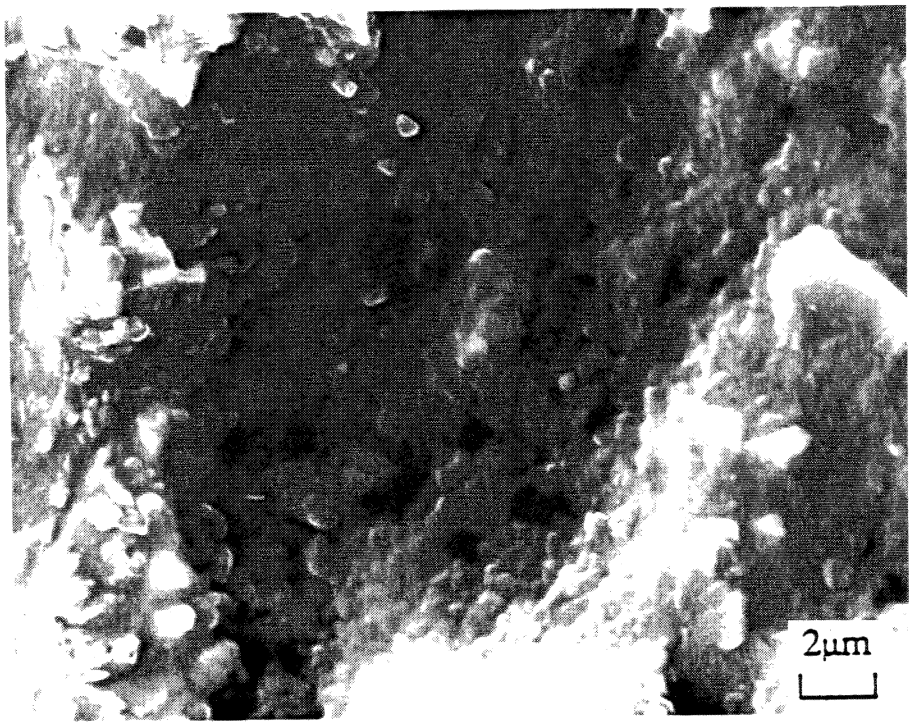

Figure 17. Scanning electron micrograph of the melting layer after the resolidification from 20-25 μm diamond.

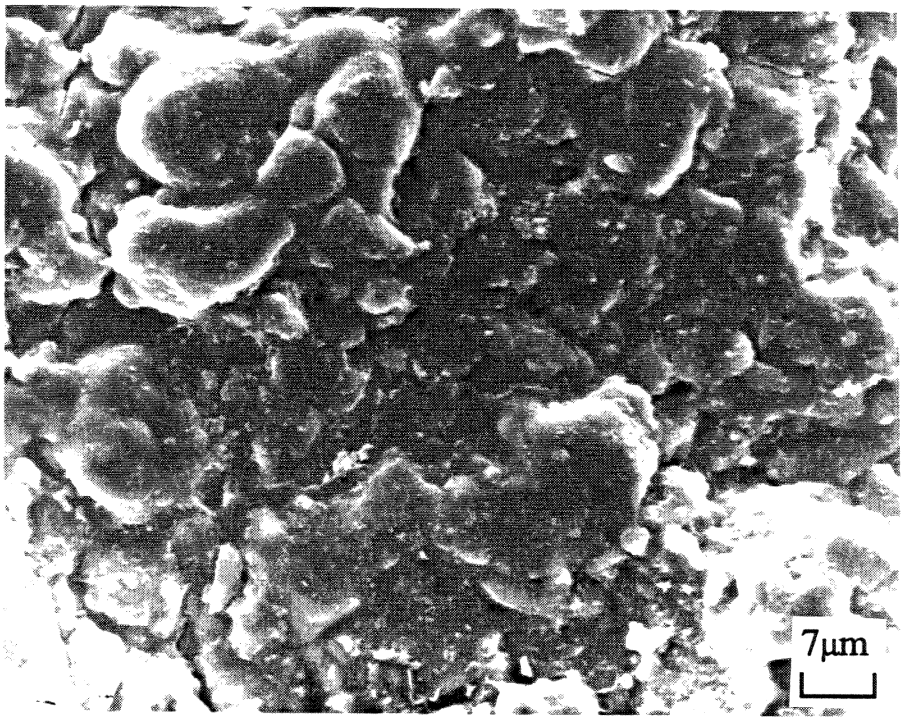

Figure 18. Scanning electron micrograph of fracture surface from consolidated 10-20 μm c-BN.

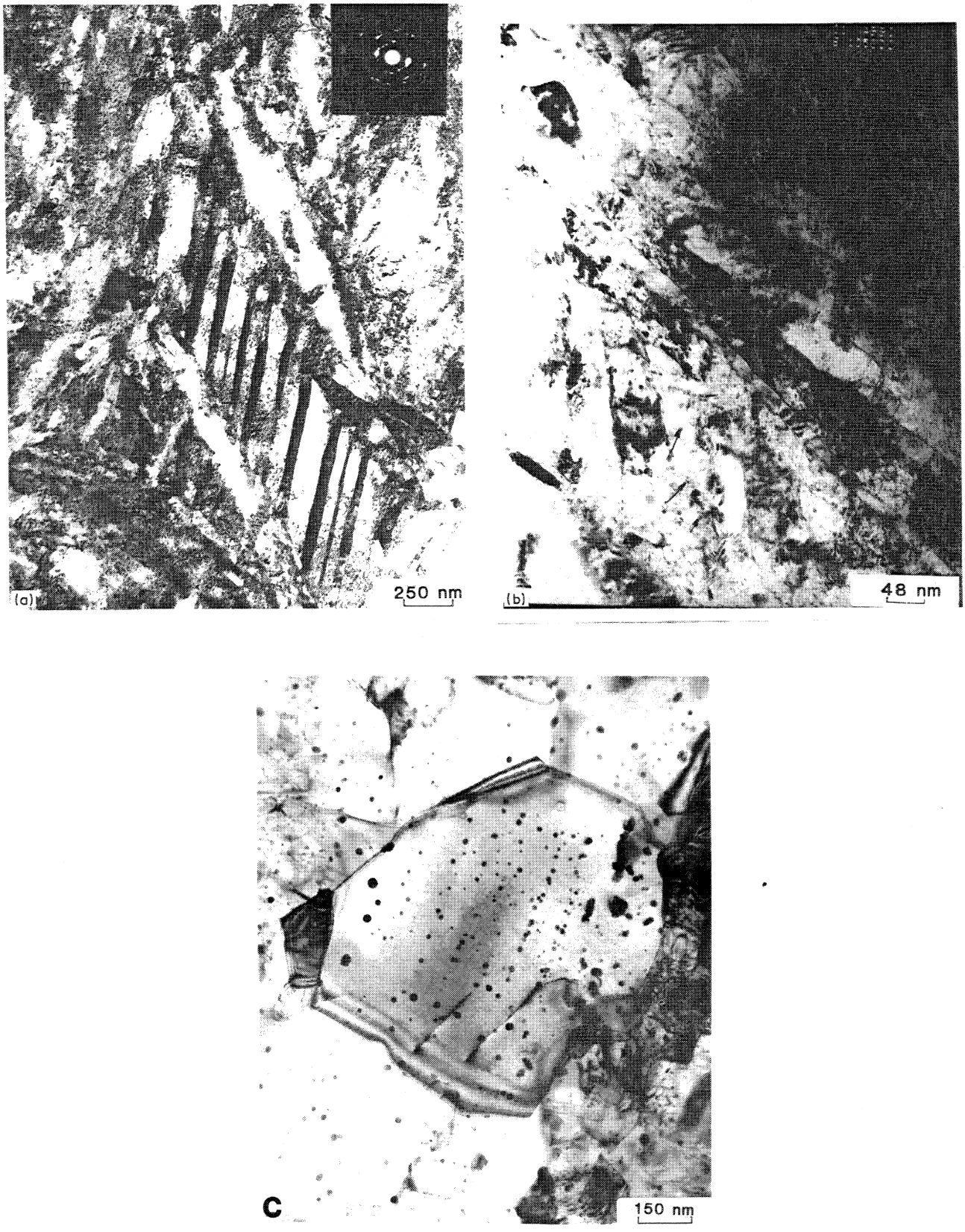

Figure 19. Transmission electron micrograph showing (a) and (b) as-shocked and (c) shocked + hipped microstructure in a titanium alloy (from Coker *et al.* [10]).

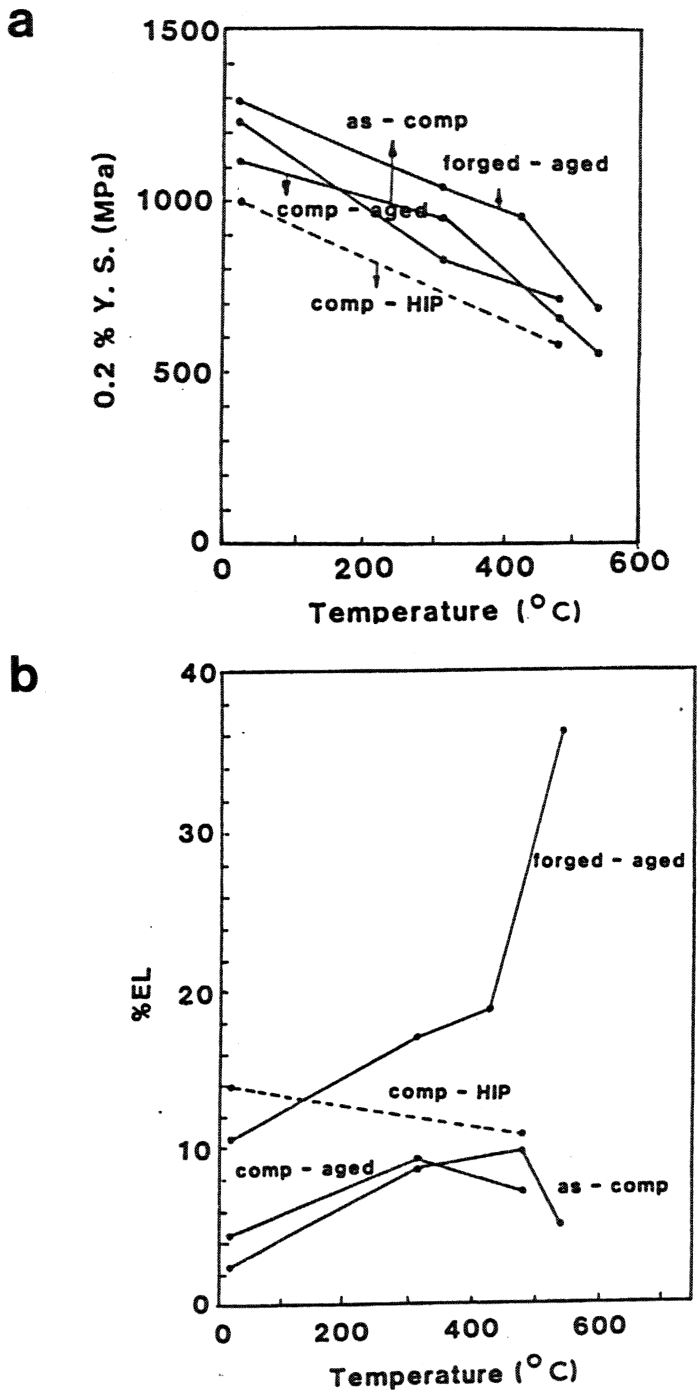

Figure 20. (a) Yield stress and (b) elongation of commercial purity titanium conventionally forged and shock (comp.) processed as a function of temperature (from Coker *et al.* [10]).

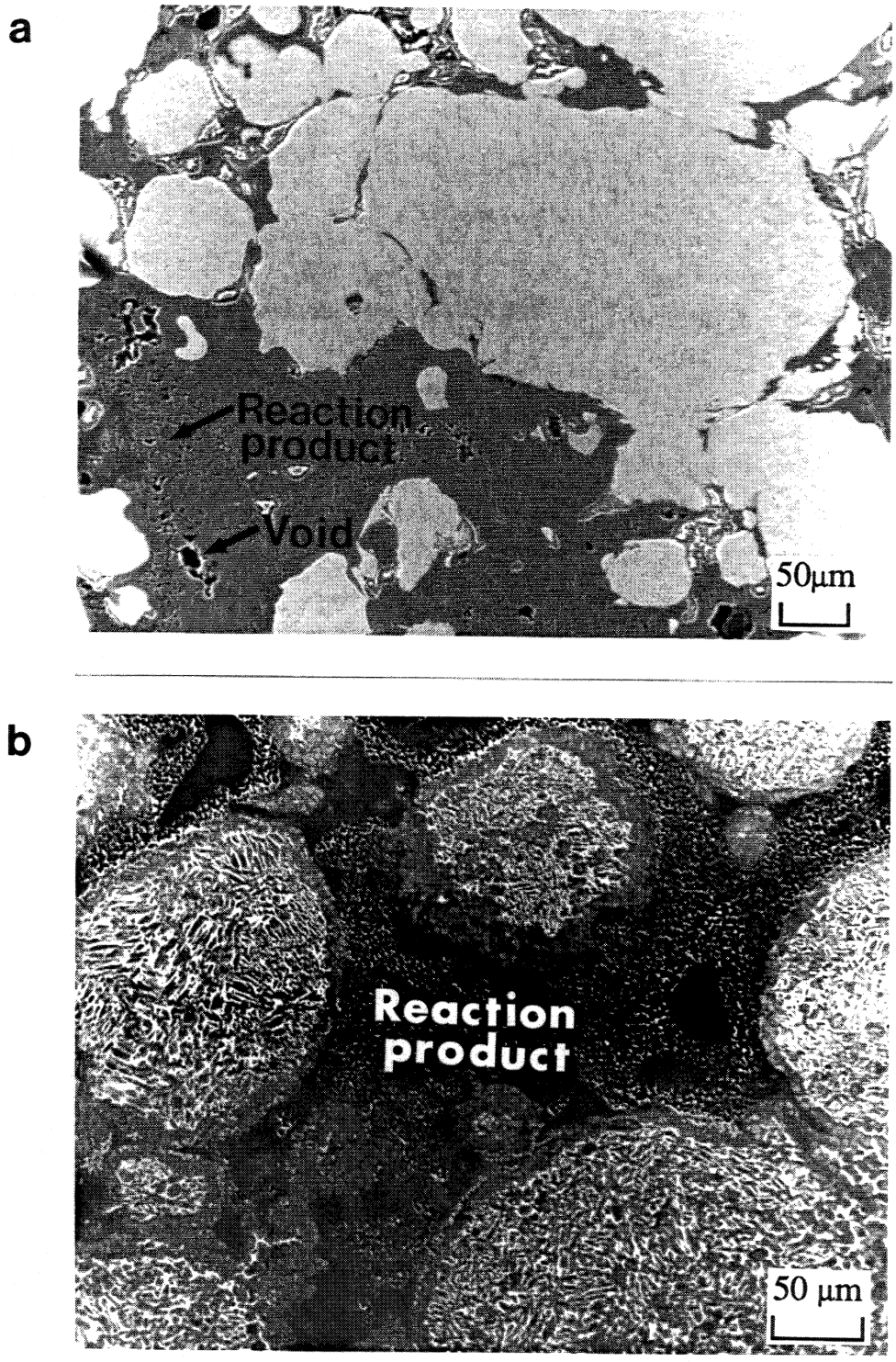

Figure 21. Scanning electron micrograph from shock-densified Ti_3Al+Ti+Al alloys (a) hipped at 600°C; (b) hipped at 1000°C at 1000°C in which the different regions were identified by EDS analysis (from Shang and Meyers[7]).

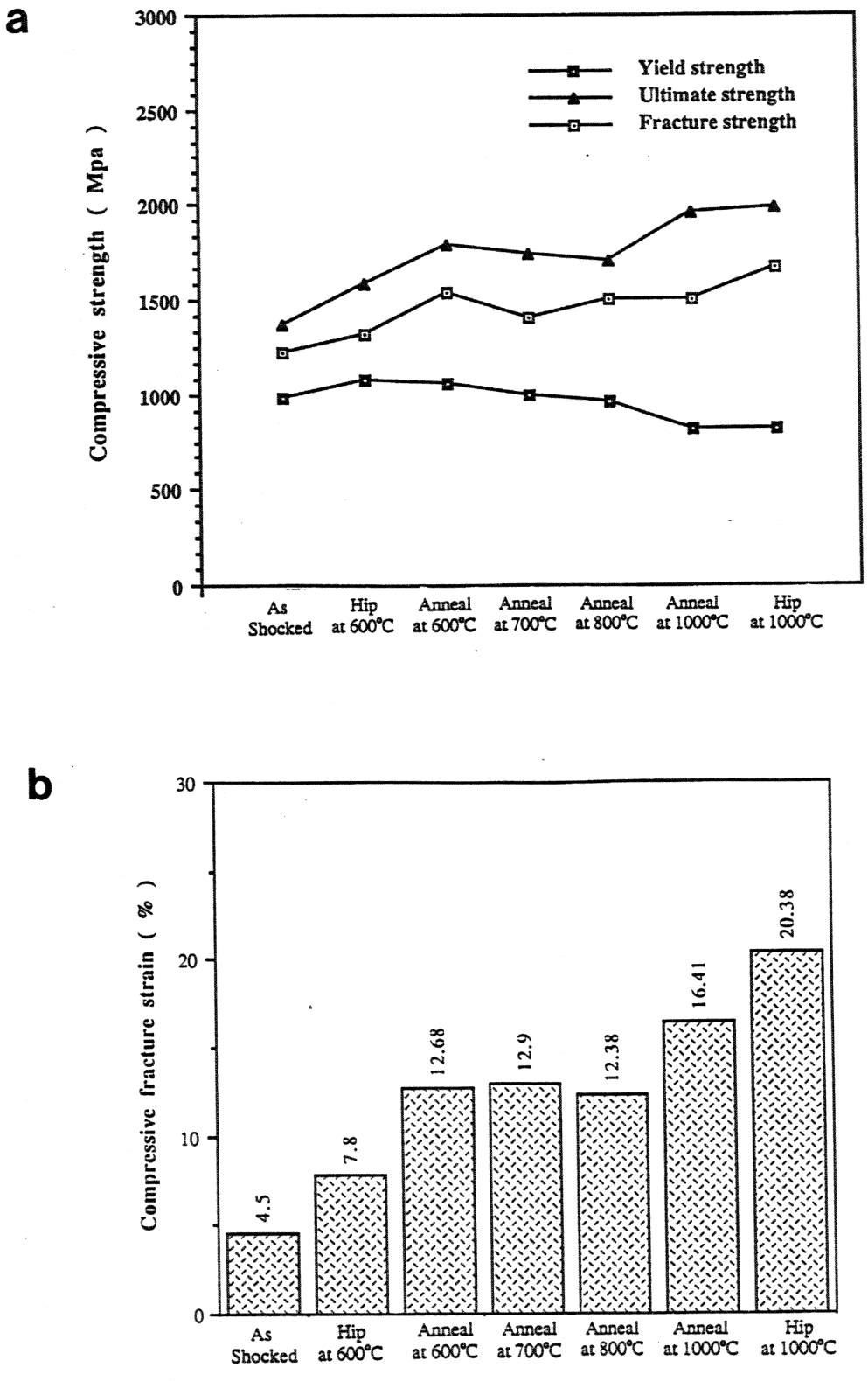

Figure 22. Compressive properties of Ti_3Al hipped or annealed from 600°C to 1000°C (a) yield strength, ultimate compressive strength, and fracture strength; (b) maximum compressive fracture strain (from Shang and Meyers[7]).

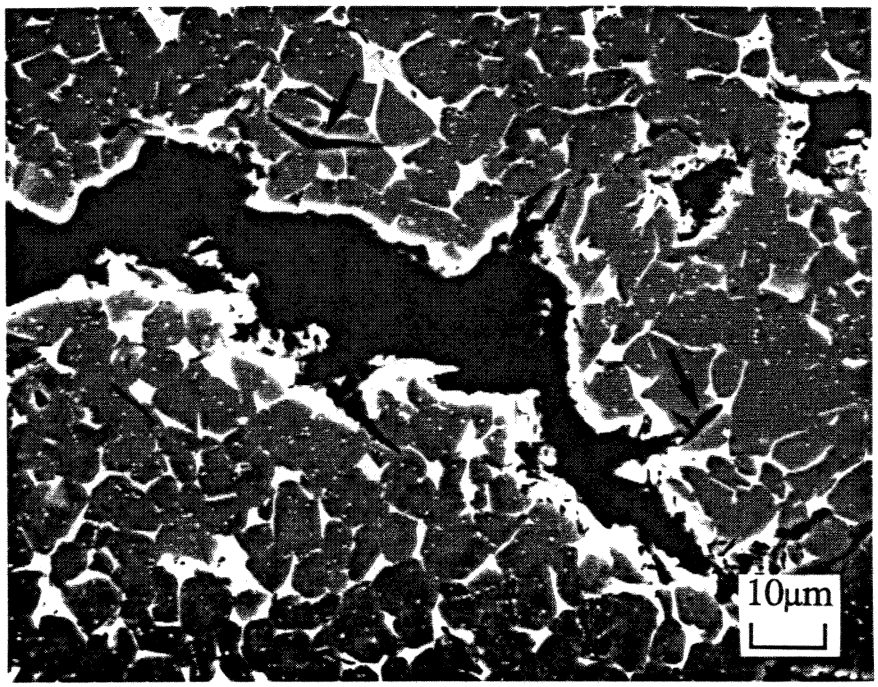

Figure 23. Scanning electron micrograph showing intergranular and transgranular cracks in the interior of Ti_3Al particle; white particles are ductile phase and dark particles are brittle phase. Arrow shows how cracks are arrested by ductile phase (from Shang and Meyers [7]).

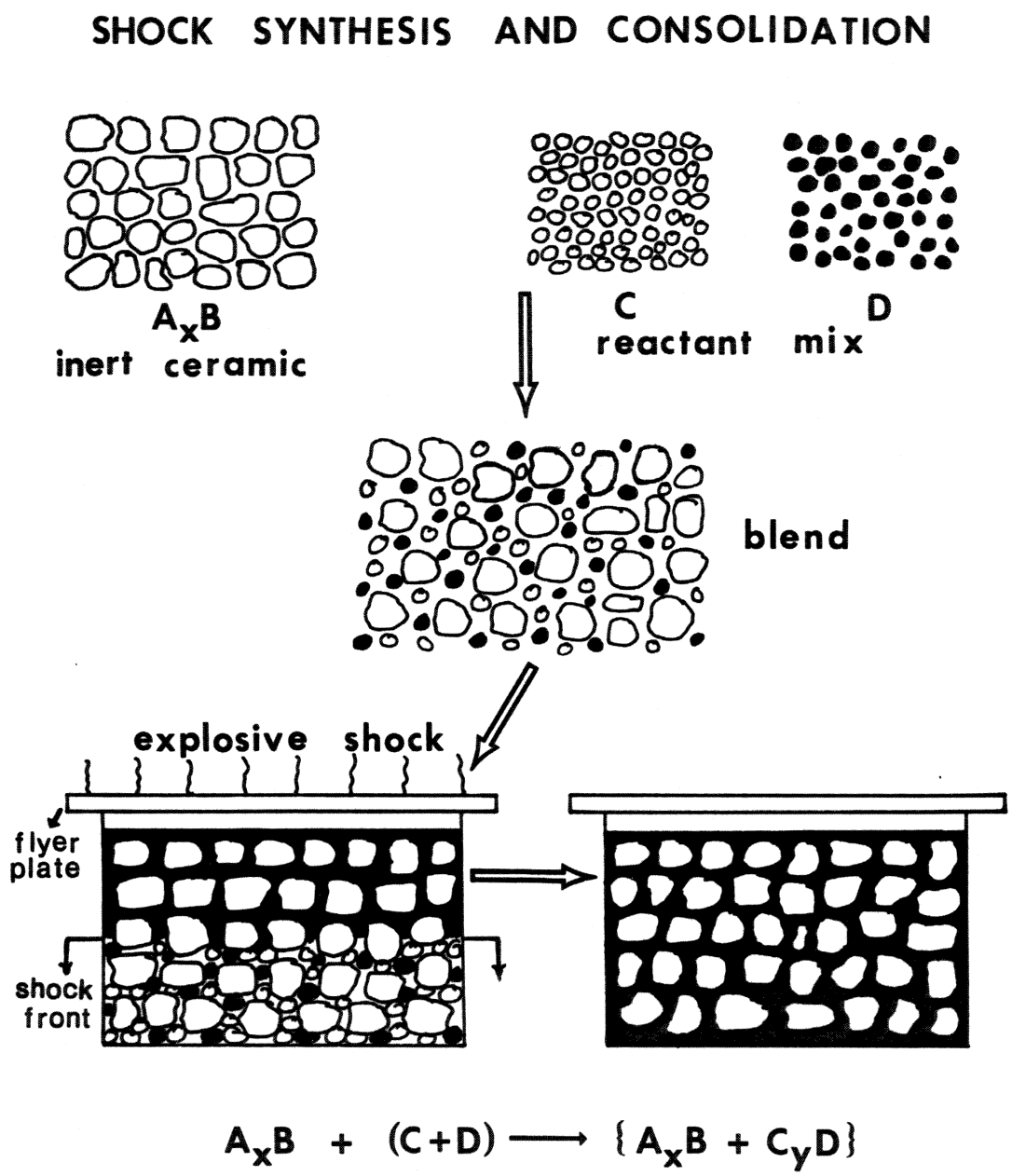

Figure 24. Sequence of events in chemically-assisted shock consolidation.

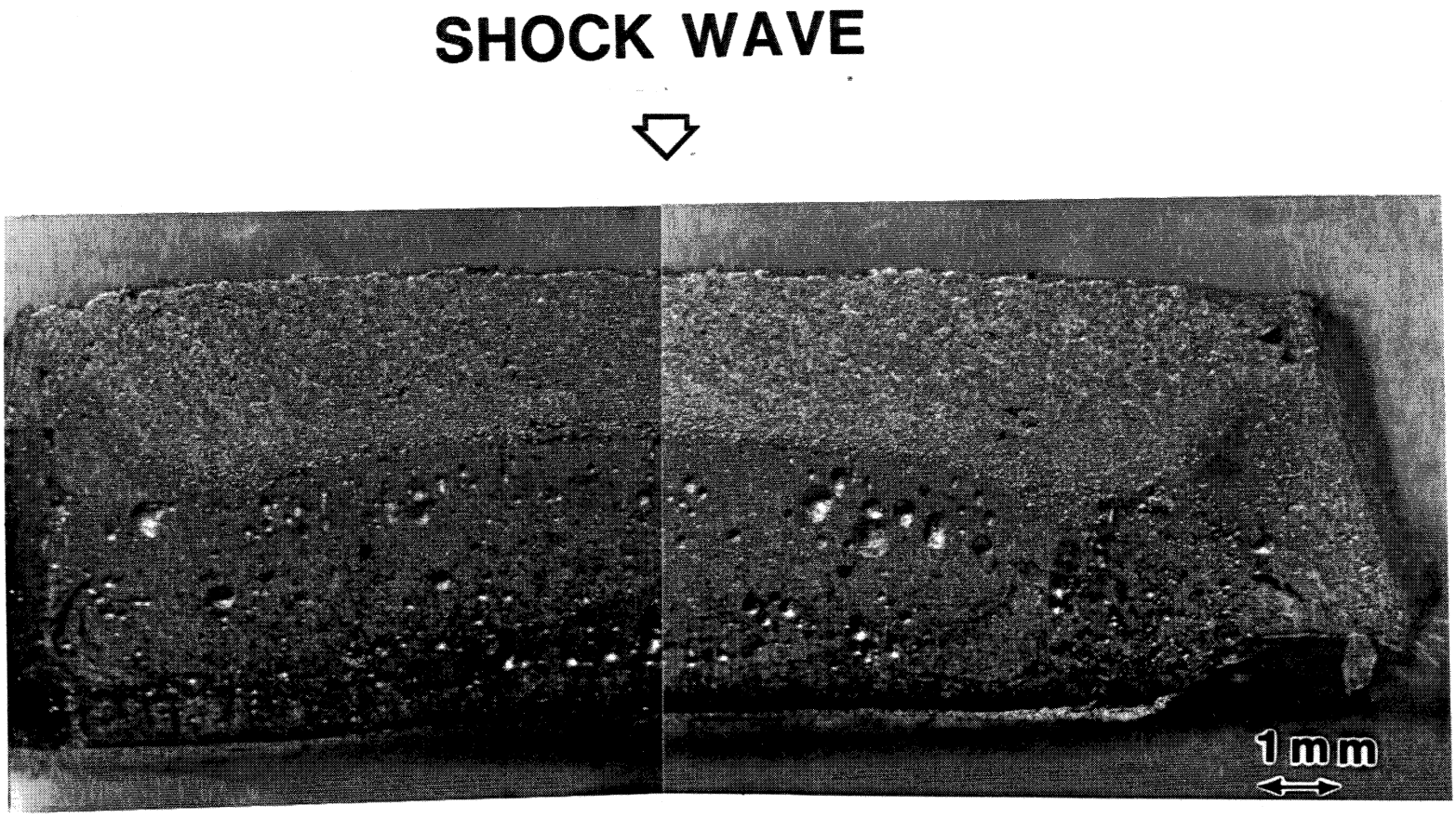

Figure 25. Typical cross-section of a shocked compact containing elemental powder reactants; notice bottom part (reacted) and top part (unreacted) (from Yu, Meyers, and Thadhani [13]).

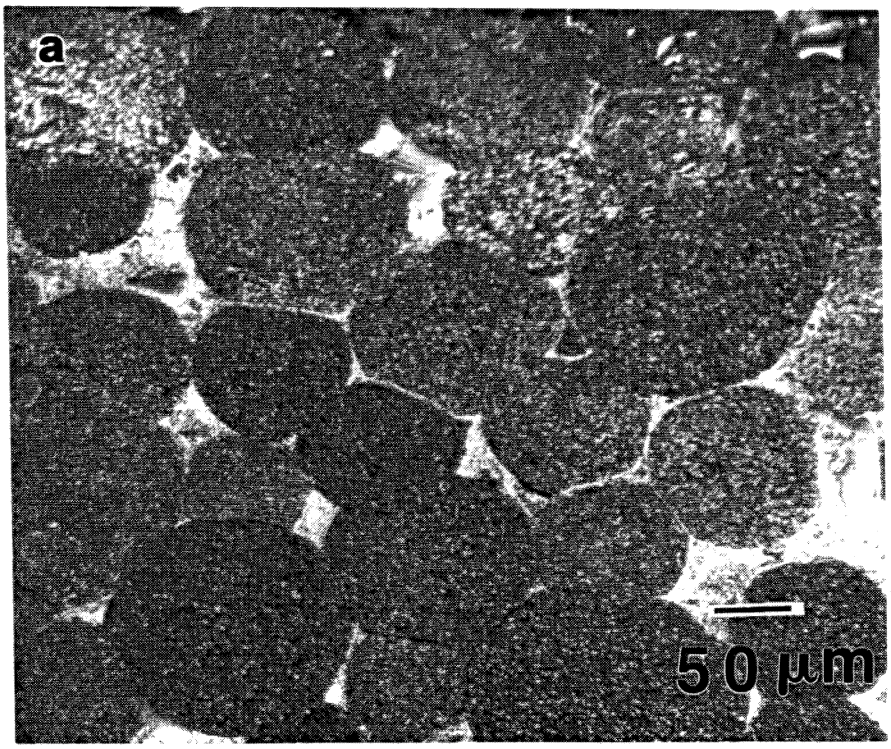

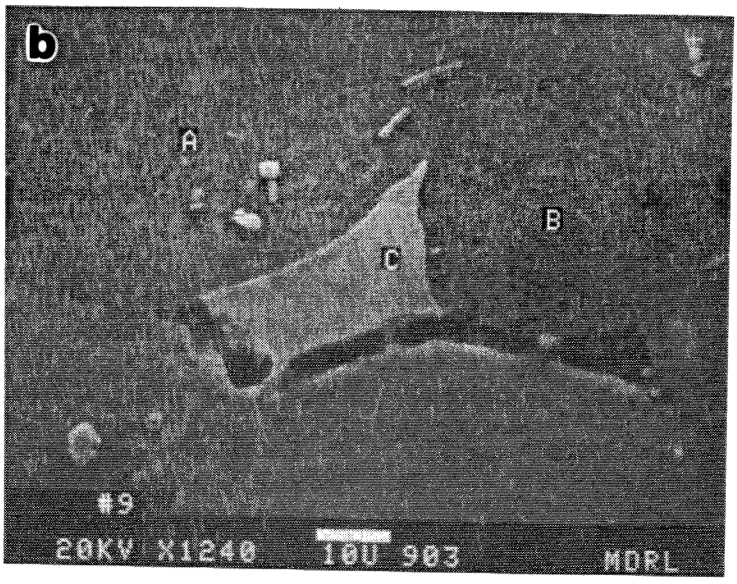

A: Al-43.2%; Ti-55.9%; Nb-0.9%
B: Al-33.9%; Ti-65.6%; Nb-0.2%
C: Nb-99.7%

Figure 26. (a) Optical micrograph of the top region of capsule containing TiAl + Nb + Al; (b) quantitative analysis of (a).

c

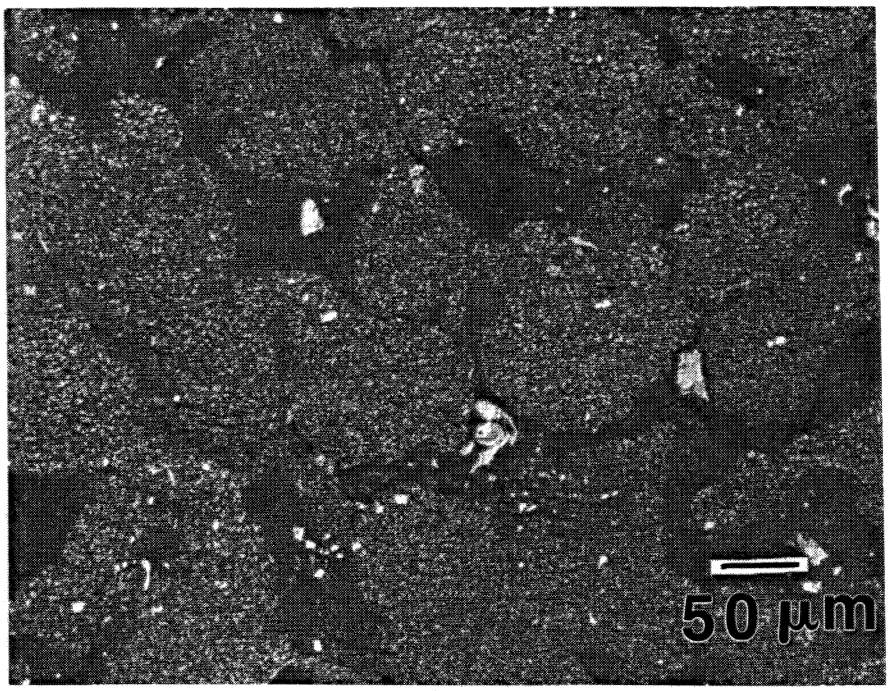

d

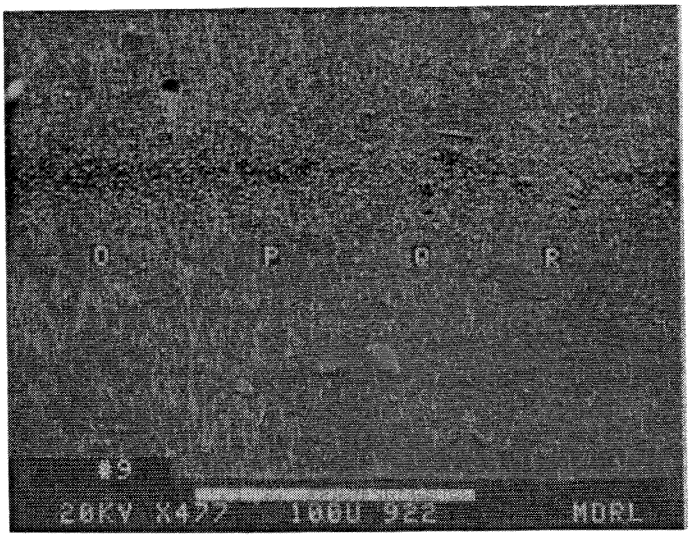

O: Al-54.3%; Ti-38%; Nb-7.6%
P: Al-53.5%; Ti-38.8%; Nb 7.7%
R: Al-53.6%; Ti-39.2%; Nb-7.2%
Q: Al-53.5; Ti-39.8%; Nb-7.2%

Figure 26. (continued): (c) Optical micrograph of the bottom region of capsule; (d) quantitative analysis of (c) (from Yu, Meyers, and Thadhani [13]).

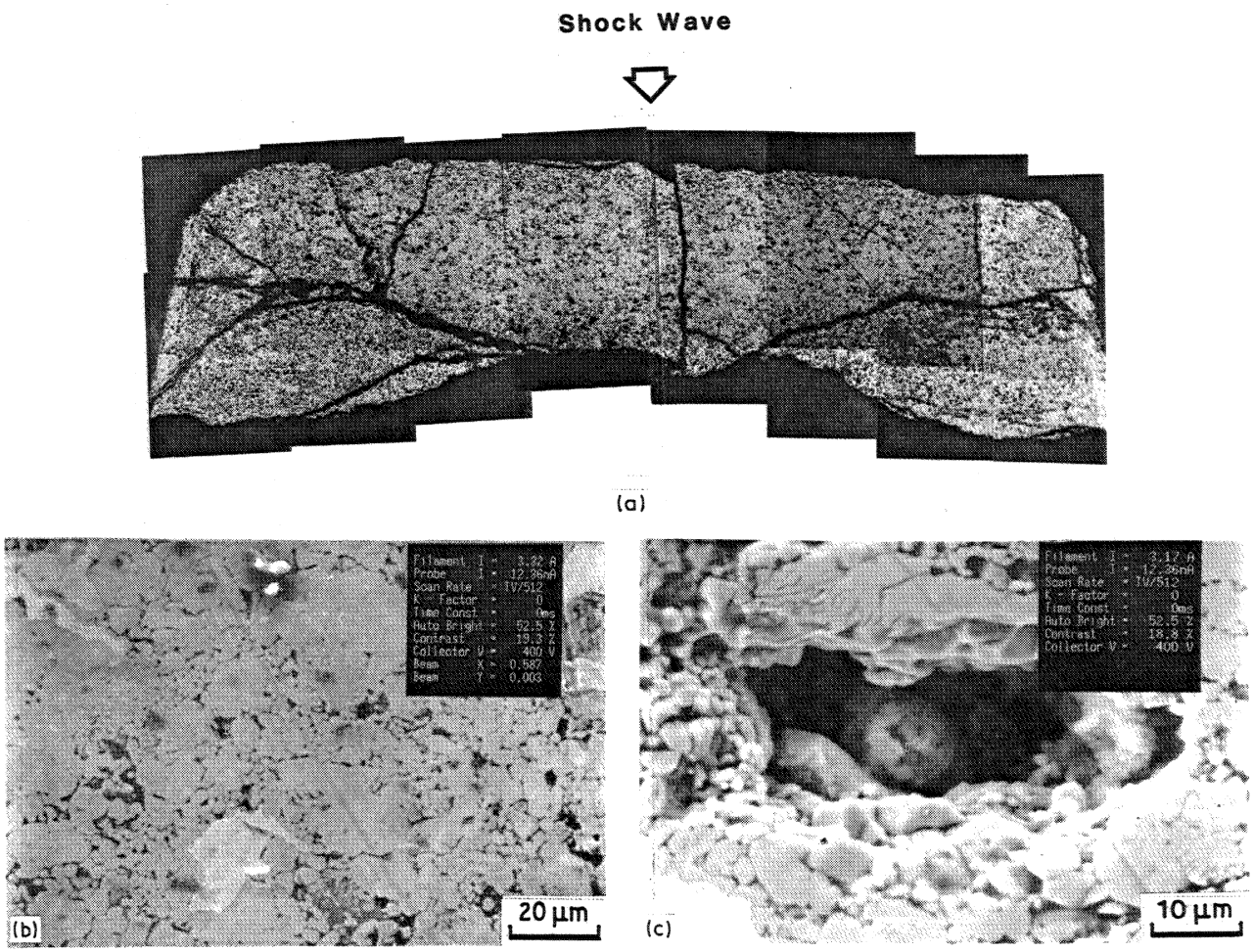

Figure 27. (a) Optical micrograph of cross-section of compact (Nb 6.2 wt%, Si 19 3.84 wt%, $NbSi_2$ 90 wt%. (b) Scanning electron micrograph of local region in (a). (c) Scanning electron micrograph of void of (a) (from Yu and Meyers [43]).

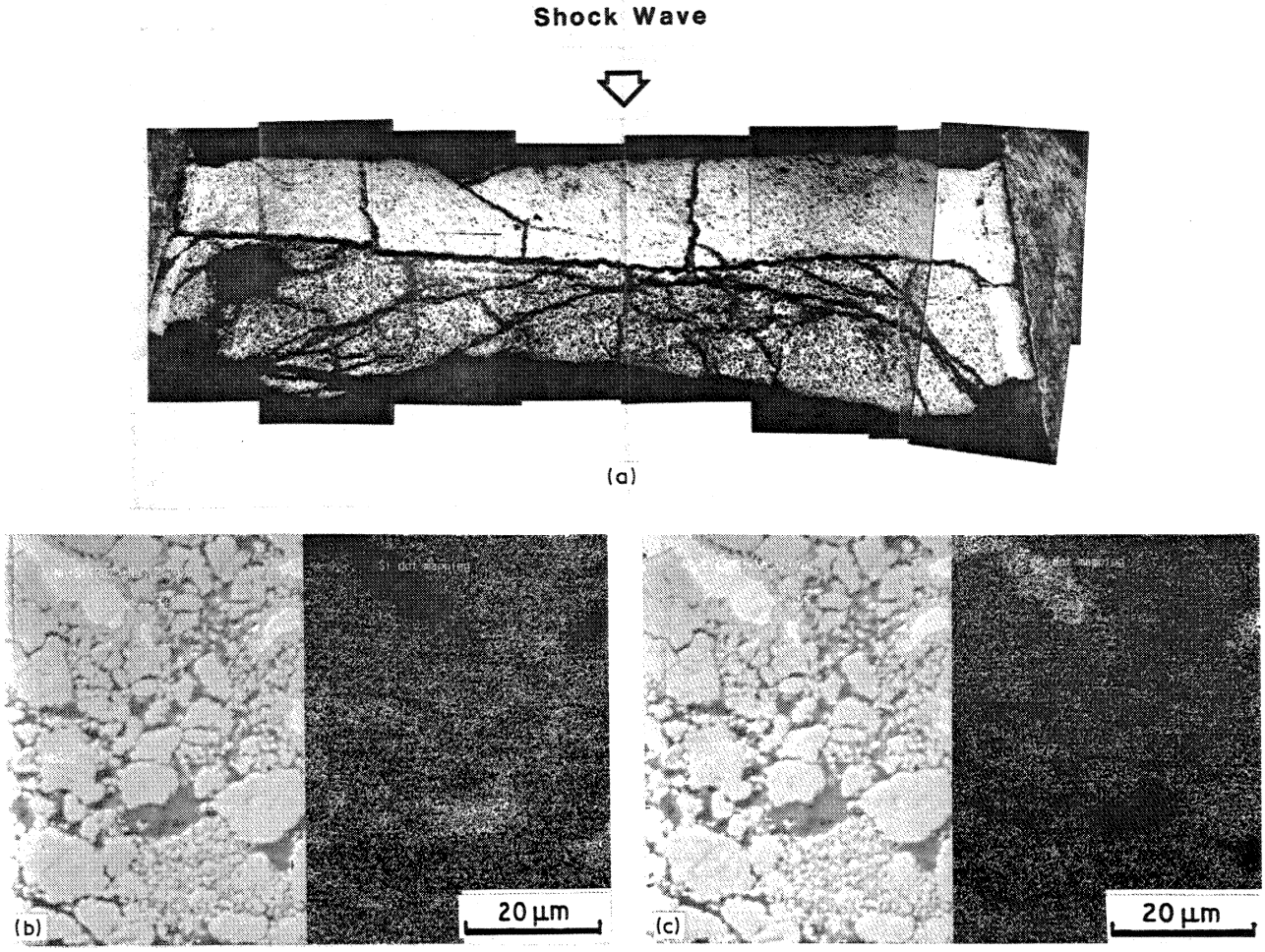

Figure 28. (a) Optical micrograph of cross-section of compact (Nb 18.6 wt%, Si 11.4 wt%, $NbSi_2$ 70 wt%). (b) Scanning electron micrograph of unreacted region, silicon dot mapping. (c) Niobium do mapping. ((d) Scanning electron micrograph of reacted region.) (From Yu and Meyers [43].)

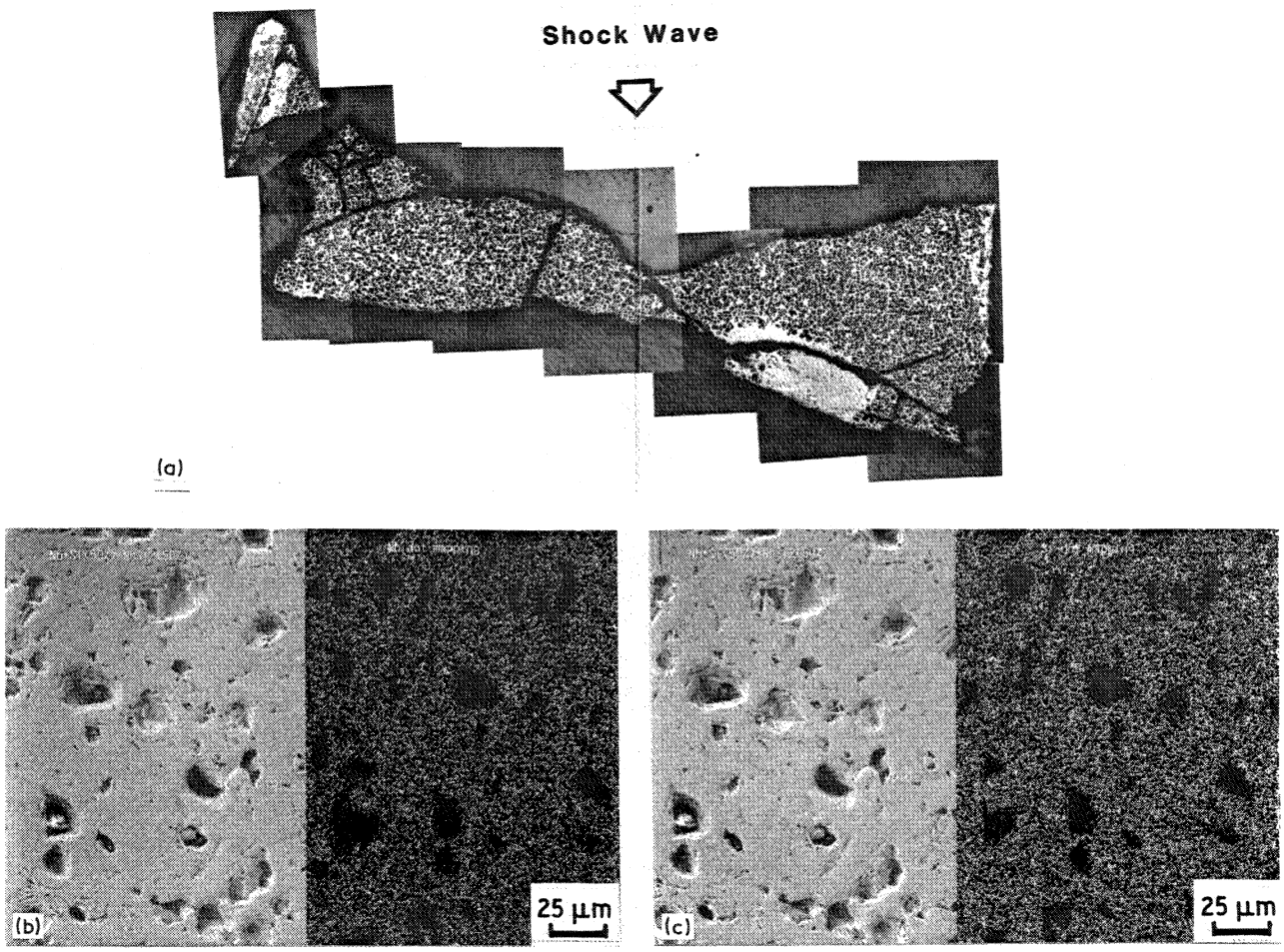

Figure 29. (a) Optical micrograph of cross-section of compact (Nb 31 wt%, Si 19 wt%, $NbSi_2$ 50 wt%). (b) Scanning electron micrograph of unreacted region, silicon dot mapping. (c) Niobium do mapping. ((d) Scanning electron micrograph of reacted region.) (From Yu and Meyers [43].)

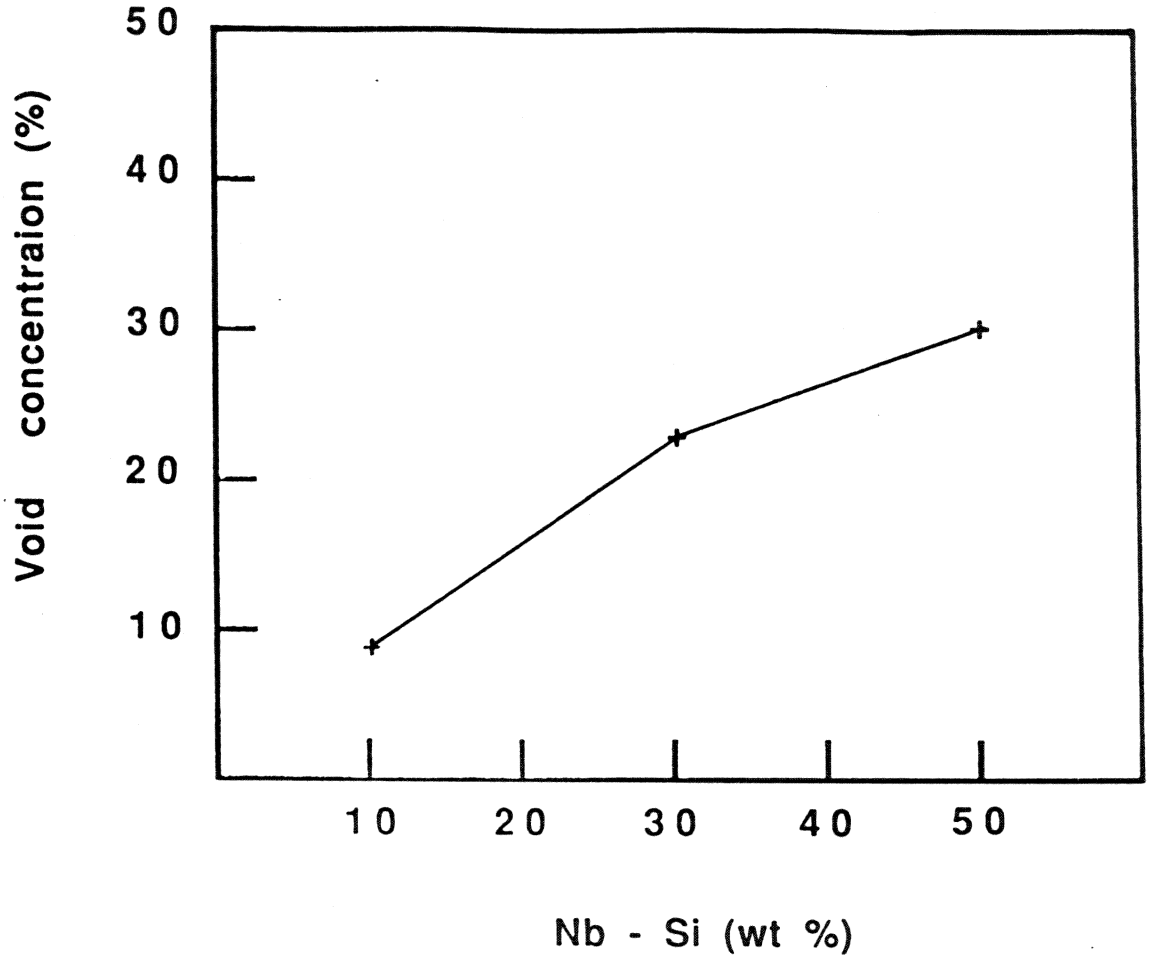

Figure 30. Void concentration plotted against Nb-Si weight percentage. (From Yu and Meyers [43].)